Sea Ice Mapping Using Enhanced Resolution Advanced Scatterometer Images

Steven Reeves

A thesis submitted to the faculty of
Brigham Young University
in partial fulfillment of the requirements for the degree of

Master of Science

David G. Long, Chair
Richard W. Christiansen
D.J. Lee

Department of Electrical and Computer Engineering

Brigham Young University

June 2012

ABSTRACT

Sea Ice Mapping Using Enhanced Resolution Advanced Scatterometer Images

Steven Reeves
Department of Electrical and Computer Engineering
Master of Science

Sea ice is of great interest due to its effect on the global climate, the Earth's ecosystem, and human activities. Microwave remote sensing has proven to be an effective way to measure many of the characteristics of sea ice. In particular, several algorithms map the daily sea ice extent using a variety of instruments. Enhanced resolution images generated from the Scatterometer Image Reconstruction (SIR) algorithm can be used to generate a high resolution ice extent map. Previous algorithms using SIR images were developed for scatterometers which are no longer operational. The Advanced Scatterometer (ASCAT) is a newer scatterometer which has different characteristics from the earlier scatterometers. The previous algorithms do not perform as well when applied to ASCAT. This thesis presents a new algorithm for ASCAT developed to discriminate sea ice from the open ocean and create daily maps of the ice extent. It is developed from previous algorithms used on earlier scatterometers. The algorithm uses an iterative Bayes decision rule to classify pixels as sea ice or ocean. Digital image processing techniques are used to reduce misclassifications. The ice maps from the new algorithm are compared with the NASA Team sea ice concentration maps from the Advanced Microwave Scanning Radiometer for the Earth Observing System (AMSR-E). The comparisons include: difference in area, distance between ice edges, number of missed and false detections. The new ice maps are also compared with the Remund-Long algorithm for the QuikSCAT satellite using the same metrics. The ice edge is verified with high resolution Synthetic Aperture Radar (SAR) data. The new ice maps perform similarly to previous ice mapping algorithms for scatterometers.

Keywords: remote sensing, sea ice, scatterometer, pattern recognition, ASCAT

ACKNOWLEDGMENTS

Many people assisted me in my research for this thesis. First, I would like to thank Dr. Long who gave me this opportunity. In addition, he gave me help when I needed it. I would also like to thank my committee for taking the time to review my research. I definitely must thank all of the students in the MERS lab who gave me lots of ideas and helped with a variety of problems. I especially would like to thank my wife for putting up with me during my research and encouraging me.

Table of Contents

List of Tables

List of Figures

Chapter 1

Introduction

Sea ice is frozen water characterized by a sheet of ice of varying thickness floating on the surface of the ocean. It is constantly changing due to melting, freezing, ocean currents, and wind. Even though sea ice occurs in some of the most remote regions of the Earth, it has a great impact on the climate, the ecosystem, and human activities.

Sea ice plays an important role in the Earth's climate. Its high albedo causes much of the sunlight that hits its surface to be reflected back into space. The reflected solar energy helps keep the polar region cool. When sea ice begins to melt, more sunlight is absorbed. This causes the area to warm up, which leads to more melting ice. Thus, sea ice impacts the Earth's radiation budget and alters the temperature of the polar regions. Areas of open water within the sea ice can lose heat rapidly causing the ice to grow. The ice formation produces dense brine which sinks into the ocean. In the reverse process, melting ice creates an influx of fresh water at the ocean's surface. Sinking brine and low density freshwater significantly affect the ocean circulation [1].

Sea ice also affects the Earth's ecosystem. Many kinds of phytoplankton thrive along the sea ice edge. During the spring time, the sea ice begins to melt creating a layer of fresh water on the ocean surface. This layer of fresh water is nutrient-rich enabling the phytoplankton to thrive. Nutrient rich water is also found within polynyas, which are open areas of water surrounded by ice. The phytoplankton serve as a food source for many small fish and krill. In addition, many types of wildlife rely on the sea ice for their habitat including seals, penguins, and polar bears [1].

Many human activities and interests rely on knowledge of sea ice. Transportation vessels and drill ships must avoid it. Knowledge about the sea ice can improve our understanding of the climate and ecosystem of the Earth. Knowing the location of the sea ice

allows the total area of sea ice to be computed. The area of the sea ice is one of the first indicators of climate change [1].

1.1 Research Problem Description

Sea ice extent is the total area covered by sea ice including open water between ice floes [2]. Many human activities including global climate studies and transportation operations benefit from knowledge of the daily ice extent. However, the daily ice extent is difficult to monitor because sea ice is constantly changing, it occurs mostly over the poles, and it covers a large area. Remote sensing overcomes many of these challenges and is frequently used to monitor the ice extent.

Remote sensing instruments used to monitor the ice extent include microwave, optical, and infrared sensors. However, optical and infrared sensors have limited capability at mapping the daily ice extent. These sensors frequently cannot see the surface of the Earth over the poles. Optical instruments rely on sunlight to illuminate the ground, and during certain times of the year, there is little sunlight that reaches the ground due to the orbit of the Earth. Clouds frequently cover many areas over the poles which also prevents sunlight from reaching the surface. Cloud cover also limits how well infrared sensors see the surface.

On the other hand, microwave sensors are well-suited for monitoring the daily ice extent. Satellite-borne microwave instruments can easily cover the polar regions in a single day. Most microwave frequencies can penetrate cloud cover and do not require the sun to illuminate the ground. Microwaves are well adapted for sensing sea ice and ocean. These advantages make microwave remote sensing instruments ideal for monitoring the sea ice extent.

Microwave sensors consist of active (radars) and passive (radiometers) instruments. Radiometers typically estimate the sea ice concentration, while scatterometers typically estimate the ice extent. The ice extent can be inferred from the ice concentration. A specific concentration value, typically 15%, is chosen such that anything greater than this concentration is considered sea ice. Some examples of sea ice concentration algorithms that use radiometers are the NASA Team (NT) [3] and the bootstrap [4] algorithms.

Space-borne passive microwave instruments have an inherently low resolution, usually 10 km per pixel or more. Although useful for many applications, it is beneficial to have an ice extent map with a better resolution.

Scatterometers are active microwave instruments originally designed to calculate wind speed and direction from backscatter measurements over the ocean. Scatterometers "see" different characteristics of the ice than radiometers, which makes them good at detecting the ice extent [5]–[10] . Although, scatterometers typically have a native resolution only somewhat better than a radiometer, the Scatterometer Image Reconstruction (SIR) algorithm enhances the resolution of scatterometer images using data from multiple passes of the instrument [11], [12].

A number of ice extent algorithms use SIR images to estimate the ice extent [5]–[7]. Of particular interest to this thesis is the Remund Long (RL) algorithm [5] and Anderson's algorithm [6]. The RL algorithm was originally developed for the NASA Scatterometer (NSCAT) and later updated to work with QuikSCAT (QSCAT). Anderson's algorithm uses QSCAT to map the ice extent.

A newer scatterometer known as the Advanced Scatterometer (ASCAT) was launched in October 2006 and is currently operational (as of April 18, 2012). ASCAT SIR images can be used with RL and Anderson's algorithm; however, better performance can be achieved with an algorithm optimized for ASCAT. The QSCAT algorithms use both horizontal and vertical polarization to help distinguish the sea ice from the ocean. Since ASCAT is single polarization, the QSCAT algorithms do not perform as well for ASCAT. In addition, QSCAT is at Ku-band which typically displays a greater contrast between ice and ocean than ASCAT which is at C-band. More significantly, ASCAT does not cover the entire polar regions in a single day, leaving gaps in the ice extent map. These challenges can be overcome with a modified ice extent algorithm for ASCAT.

1.2 Thesis Statement

This thesis presents a new method to map the ice extent using enhanced resolution ASCAT images. The new method is a modified version of RL [5] and Anderson's [6] algorithms. The new algorithm incorporates a prior into the decision rule, and the algorithm

uses a new image type that shows azimuth modulation. The addition of the prior and the image allow the algorithm to more accurately map the ice extent. In addition, data gaps from daily ASCAT images are classified using the previous day's ice map to give a spatially consistent ice map.

1.3 Research Contributions

This thesis presents three main research contributions:

1. A new algorithm is developed to detect and map sea ice using enhanced resolution ASCAT images.

2. A new image type that shows azimuth modulation is developed.

3. A novel method is developed and used to compare the sea ice edges predicted using different ice extent algorithms.

The new algorithm uses an iterative Bayes decision rule to classify pixels as sea ice or ocean. The decision rule uses both a prior and a conditional PDF to decide whether a pixel is sea ice or ocean. A prior is generated from the previous day's ice map and a thresholded image, and the conditional PDF is estimated empirically. To correct errors in the initial classification, the last part of the algorithm uses minimal digital image processing to finalize the ice maps.

The ice maps produced by the new algorithm are validated by comparison to ice maps from other algorithms. Multiple metrics provide an objective way to determine how well two ice maps agree. One metric is to compare the areas of the two ice maps. Since we are particularly interested in the ice edge, it is also useful to compare how well the two ice edges agree. The second metric computes the average distance between two ice edges.

The ice maps generated by the new algorithm are validated with the AMSR-E NT ice maps and the RL ice maps. The new algorithm performs well when compared to both datasets. With both datasets, the new ice maps had a less than 15% percentage error in area. The algorithm's performance is seasonal, where better performance is seen during the winter time. The new ice maps also perform well when compared to high resolution SAR data.

1.4 Thesis Outline

This thesis is outlined as follows: First, the necessary background is given in Chapter 2, including microwave remote sensing, the SIR algorithm, and ice mapping algorithms. Following that, Chapter 3 describes the new approach for detecting sea ice using ASCAT, and Chapter 4 discusses tuning the algorithm for best performance. The new algorithm is then compared with the RL ice masks, the NT ice maps, and high resolution SAR images in Chapter 5. Finally, Chapter 6 concludes and provides suggestions for future research.

Chapter 2

Background

This chapter provides background information necessary for the rest of the thesis. First, microwave remote sensing using active and passive instruments is described. Next, Section 2.2 gives an overview of the Scattorometer Image Reconstruction (SIR) algorithm that enhances scatterometer images. Finally, Section 2.3 presents a few ice mapping algorithms that are relevant to this thesis.

2.1 Microwave Remote Sensing

Microwave remote sensing uses microwaves to extract information about the Earth. This section presents two types of microwave remote sensing instruments: active and passive.

2.1.1 Active Microwave Instruments

Active microwave instruments transmit a pulse of electromagnetic energy in the microwave region of the electromagnetic spectrum. The pulse illuminates a scene on the earth which reflects some of the energy back to the instrument. Assuming that there are many point scatterers with no one scatterer dominating, the power received at the instrument is related to the power transmitted through the monostatic radar equation:

$$P_r = \frac{P_t G^2 \lambda^2 A}{(4\pi)^3 R^4} \sigma^\circ, \tag{2.1}$$

where P_t is the transmitted power, P_r is the received power, G is the antenna gain, λ is the wavelength of the pulse, A is the area illuminated on the surface of the earth, R is the slant range to the target, and σ° is the normalized radar cross section (NRCS) of the illuminated area. The NRCS depends on the properties of the illuminated scene, as well as

properties of the transmitted pulse. The scene affects the NRCS through the permittivity, surface geometry, and below the surface scattering (volume scattering). The radar affects the NRCS through the frequency, incidence and azimuth angles, and the polarization of the transmitted pulse. The goal of many active microwave instruments is to estimate σ° using Eq. (2.1).

The two main types of active microwave instruments of interest to this thesis, are scatterometers and synthetic aperture radar (SAR). Scatterometers are highly calibrated instruments that can accurately measure σ°. They estimate wind speed and direction over the ocean by measuring σ° at a variety of azimuth and incidence angles. In addition to estimating wind vectors, scatterometers are also used to study land and ice, including the polar regions. Scatterometers have frequent coverage of the poles, usually several times a day.

SAR is much like a scatterometer in that it images σ°. However, using the relative motion between the target and the instrument, a SAR is able to generate a much higher resolution image. The trade-off is much more limited coverage when compared to a scatterometer. This paper uses SAR images to subjectively verify the location of the sea ice. Next, two scatterometers are described in detail.

Advanced Scatterometer

The Advanced Scatterometer (ASCAT) instrument is a fan beam scatterometer launched on the MetOp-A satellite in October 2006 and is currently operational (as of April 18, 2012). It employs six fan beam antennas with three on each side all operating at 5.255 GHz (C-band) and vertical polarization. These antennas are in a fixed position. The movement of the spacecraft creates a swath on either side. The measurement geometry for ASCAT is shown in Figure 2.1. The swath on either side is 550 km with a nadir gap in the middle. The incidence angle ranges from 25 to 65 degrees. It takes 29 days for ASCAT to have an exact-repeat orbit, and 5 days for near-repeat orbit [13].
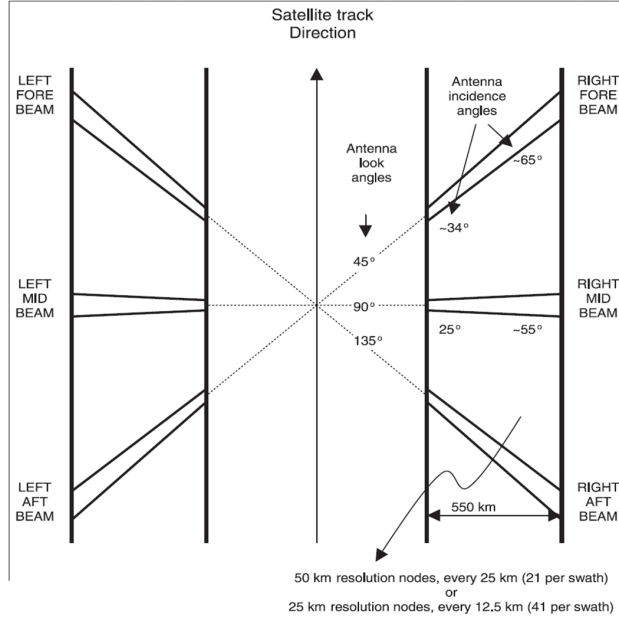
Figure 2.1: ASCAT measurement geometry [13].

QuikSCAT

The SeaWinds scatterometer aboard the QuikSCAT (QSCAT) satellite was operational from July 1999 to November 2009. In this paper, it is referred to as QSCAT to avoid confusion with the short-lived SeaWinds instrument aboard ADEOS-II. QSCAT uses a dual pencil beam that is scanned conically as the instrument moves along its orbit path. Both beams operate at 13.4 GHz (Ku-band) at an approximately constant incidence angle. The outer beam is at an incidence angle of 55° and vertical polarization, and the inner beam is at an incidence angle of 47° and horizontal polarization. The scanning geometry of QSCAT is shown in Figure 2.2. QSCAT covers 90% of the Earth every day including all of the poles except a small area directly over the pole that is never covered.

QSCAT's instantaneous antenna footprint on the ground has a nominal resolution of approximately 25 km azimuth by 35 km in the range direction. This measurement footprint is termed an "egg". The "eggs" are further resolved into "slices" through range and Doppler processing. Each egg consists of twelve slices which are about 6 km in the range direction by 25 km in azimuth [15]. This thesis uses the egg resolution only since it matches better with ASCAT.
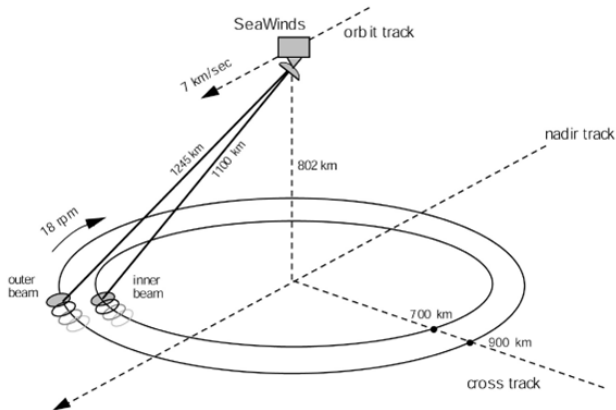
Figure 2.2: QSCAT scanning geometry [14].

2.1.2 Passive Microwave Instruments

Passive microwave instruments (radiometers) measure electromagnetic radiation naturally emitted from objects. All matter with a temperature above absolute zero radiates electromagnetic energy. Brightness temperature, T_B, is the parameter of interest in radiometers. Brightness temperature is related to the physical temperature of an object by emissivity

$$T_B = eT_p, \tag{2.2}$$

where T_p is the physical temperature of the object and e is the emissivity. The emissivity is a function of the material, the incidence and azimuth angles, the frequency, the polarization, and the surface geometry. It ranges from 0 to 1, with a 1 meaning $T_B = T_p$, while an emissivity of 0 means the material is non-emitting. The brightness temperature observed at the antenna consists of emissions from the ground, scattered emissions from down-welling radiation from the atmosphere, upwelling radiation from the atmosphere, and noise from the receiver system. In practice, the estimated noise from the receiver system is subtracted from the apparent temperature seen at the antenna. However, emissions from upwelling and down-welling radiation are difficult to estimate. At lower microwave frequencies, the atmosphere is effectively transparent, and thus does not contribute much to the estimated brightness temperature of the scene. At higher frequencies, water vapor absorption bands

9

(around 22 GHz and 183 GHz), and oxygen absorption bands (50-70 GHz and 119 GHz), in the atmosphere contribute to the apparent brightness temperature.

Though emissivity is partly a function of instrument parameters (frequency, polarization, incidence angle, etc.), the brightness temperature contains much information about the scene. Radiometers have been used for a wide range of applications including determining sea surface temperature, wind speed, sea ice concentration, snow depth, and rain rates.

AMSR-E

The Advanced Microwave Scanning Radiometer on the Earth observing system (AMSR-E) is a total power radiometer aboard the Aqua satellite which was launched in May 2002. The scanning geometry for AMSR-E is shown in Figure 2.3. It has six frequencies with both horizontal and vertical polarization. The antenna is conically scanned at an incidence angle of $55°$ and swath width of 1450 km. AMSR-E frequently covers the polar region of the earth except for a small gap directly over the poles. AMSR-E is widely used in polar studies [16]–[19].
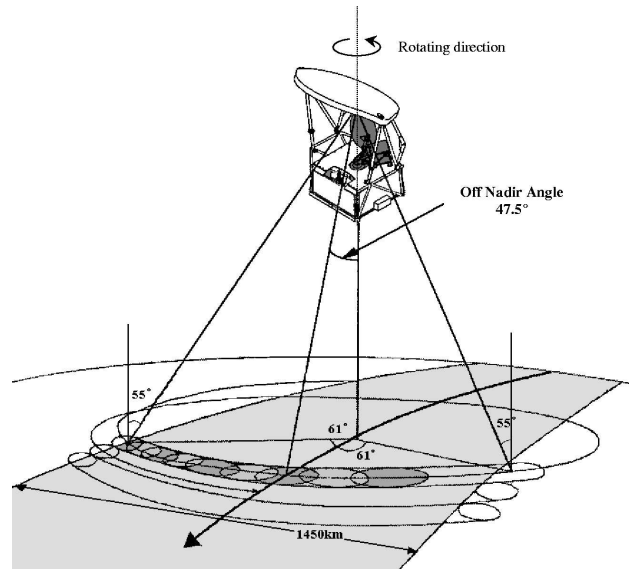

Figure 2.3: Scanning geometry for AMSR-E [17].

2.2 Image Enhancement

Scatterometers and radiometers have an inherently low resolution, usually on the order of tens of kilometers. Though useful for many remote sensing applications on a large global scale, many applications require a higher resolution. The Scatterometer Image Reconstruction (SIR) algorithm is an iterative block multiplicative algebraic reconstruction procedure that uses data from multiple passes of an instrument to generate a high resolution image of the surface backscatter [11], [12]. The sampling is irregular, meaning that it is not an even grid. The SIR algorithm uses the irregular sampling to extract information from the side lobes of the antenna pattern in the spatial frequency domain which increases the spatial resolution. In addition, the image is reproduced on a regular grid. The SIR algorithm trades temporal resolution for increased spatial resolution.

For fan-beam scatterometers, the SIR algorithm relies on a linear relationship between $\sigma°$ and incidence angle:

$$\sigma°(\theta_i) = \mathcal{A} + \mathcal{B}(\theta_i - \theta_{ref}), \tag{2.3}$$

where θ_i is the incidence angle, $\sigma°(\theta_i)$ is the NRCS in dB, θ_{ref} is a reference angle usually $40°$, and $\mathcal{A}$ and $\mathcal{B}$ are constants that depend on the scene. $\mathcal{A}$ represents the average $\sigma°$ over the imaging interval at the reference angle. The $\mathcal{B}$ coefficient accounts for the dependence of the scene on incidence angle. The SIR algorithm requires that the true $\sigma°$ value does not change during the imaging interval, an assumption which is not always true. The ocean is very dynamic and constantly changing. The $\sigma°$ value over the ocean depends on the near surface winds which can change many times a day. In addition, $\sigma°$ over certain areas can change with the azimuth angle [20], [21]. The backscatter can change due to many other factors as well. However, many areas of the Earth over land and ice are relatively constant in $\sigma°$ during the imaging interval. SIR images have been used in many land and ice studies [6], [22]–[24].

Images of the $\mathcal{A}$ and $\mathcal{B}$ estimates are created from the $\sigma°$ measurements for ASCAT at vertical polarization only. The images are gridded at 4.45 km per pixel. An example of $\mathcal{A}$ and $\mathcal{B}$ images for ASCAT is shown in Figure 2.5. Note the black diamonds on both images

which are areas that ASCAT does not cover in a single day. ASCAT does not have as much coverage as QSCAT due to the fan beam design with its narrow swath and nadir gap.

For QSCAT, the $\mathcal{B}$ image is not created since QSCAT is at a constant incidence angle. $\mathcal{A}$ images are created for both horizontal and vertical polarizations for QSCAT. QSCAT egg images are gridded at a 4.45 km pixel resolution, and slice images are gridded at 2.225 km. An example of an $\mathcal{A}$ egg image for both vertical and horizontal polarization is shown in Figure 2.4. The equivalence of the ASCAT and QSCAT egg grids allow for a direct comparison between the images. This allows the ice maps from the new algorithm to be directly compared to the QSCAT ice maps.
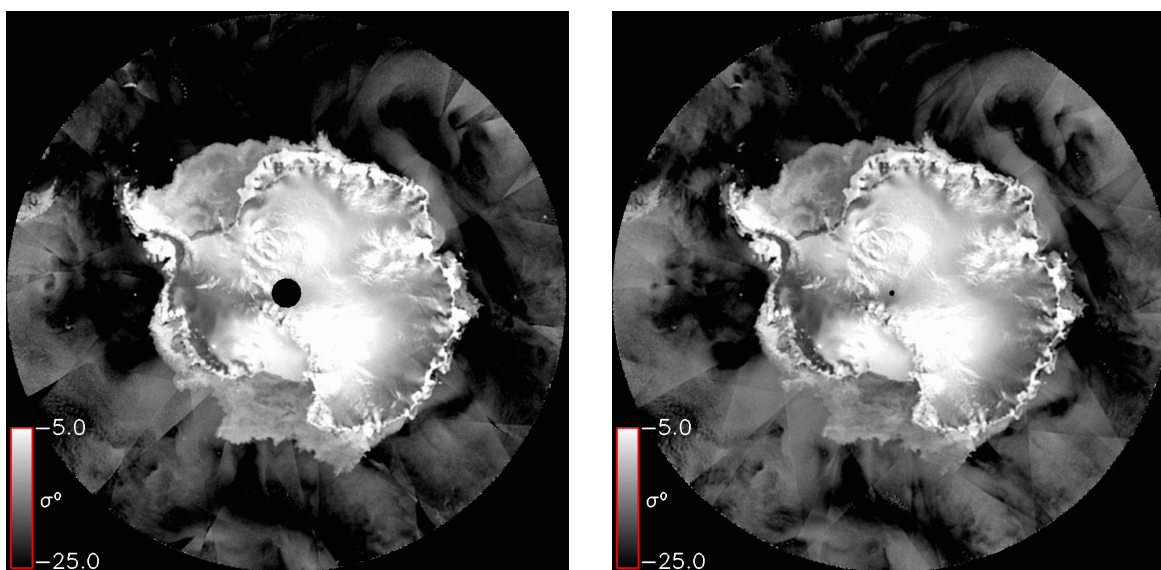
(a) QSCAT $\mathcal{A}$ horizontal image   (b) QSCAT $\mathcal{A}$ vertical image

Figure 2.4: $\mathcal{A}$ egg images for QSCAT on March 21, 2009 over Antarctica.

In addition to $\mathcal{A}$ and $\mathcal{B}$ images, ancillary images are produced by the SIR algorithm. These give information regarding the number of measurements per pixel, incidence angle, collection time, and variance in σ°. Of particular interest to this thesis is the variance (V) image. These images are the variance of the difference in the σ° of each pixel with the forward projections of the σ° measurements. It is important to note that σ° is in dB when
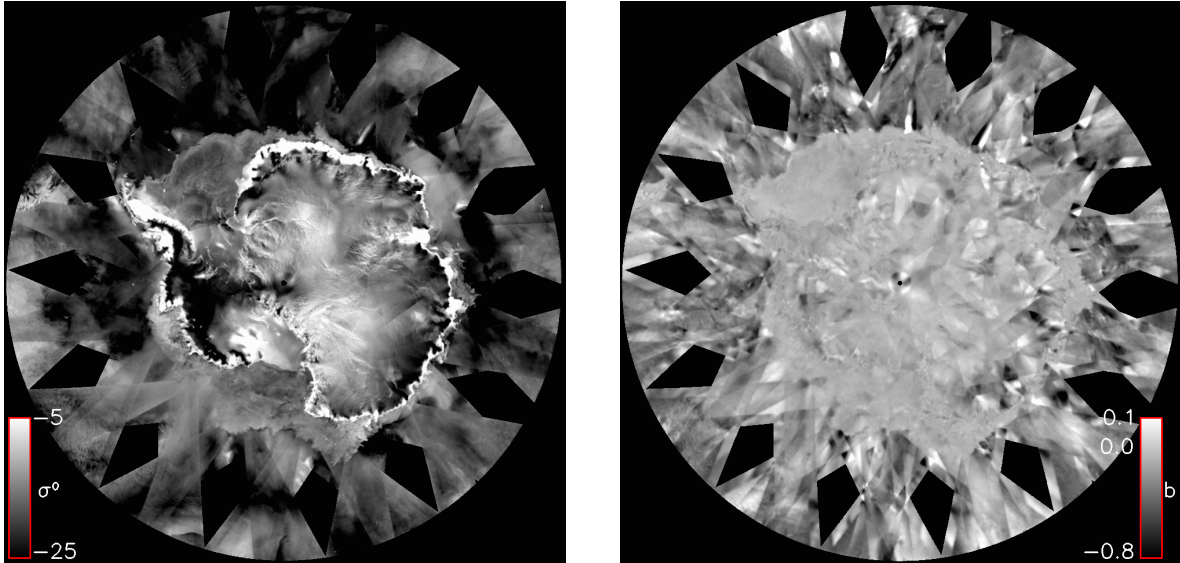
(a) ASCAT $\mathcal{A}$ image

(b) ASCAT $\mathcal{B}$ image

Figure 2.5: $\mathcal{A}$ and $\mathcal{B}$ images for ASCAT on March 21, 2009 over Antarctica.

computing this variance. The V images represent changes in the observed σ° during the imaging interval due to variations in time, incidence angle, and azimuth angle. V images for QSCAT and ASCAT are shown in Figure 2.6.

2.3   Ice Mapping Algorithms

Several ice mapping algorithms have been developed for a variety of instruments. Algorithms developed for passive instruments include the NASA Team (NT) [3] and the bootstrap [4] algorithms. These algorithms estimate the sea ice concentration at resolutions of 12.5 km per pixel or coarser.

Many algorithms also exist for scatterometer data [5]–[10]. Rivas et. al. [8] uses a wind and sea ice model function to detect sea ice with QSCAT. Park et. al. [9] uses neural networks to map the ice with NSCAT. Gohin et. al. [10] create images that show azimuth and incidence angle dependence to detect sea ice with the ERS-1 scatterometer. These algorithms create ice maps at the native resolutions of the respective instruments (25 km and worse).
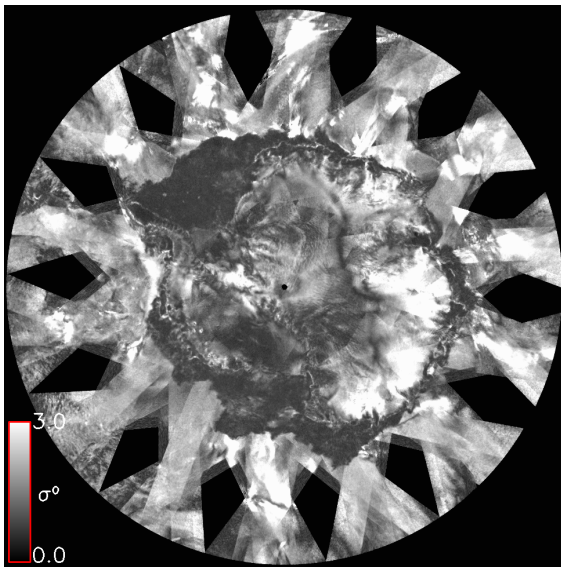
(a) ASCAT V image
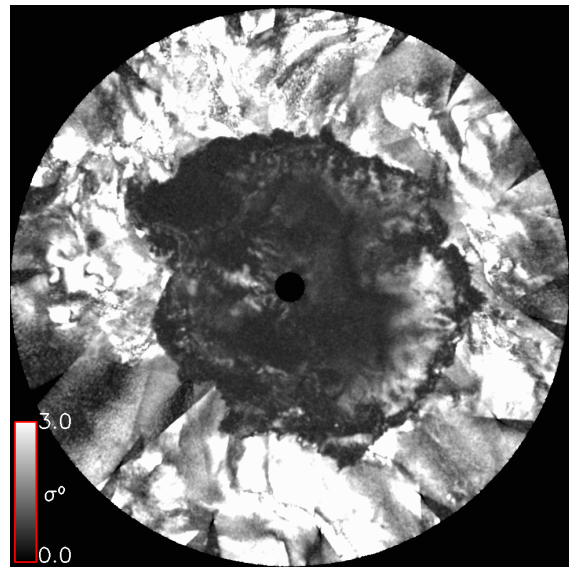
(b) QSCAT V horizontal image
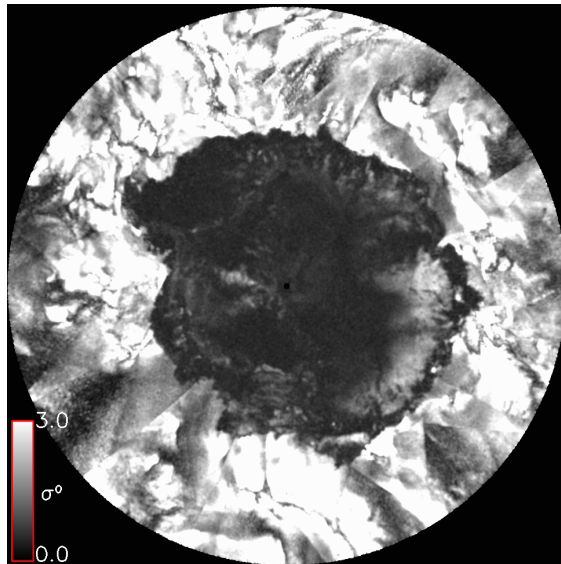
(c) QSCAT V vertical image

Figure 2.6: V images for ASCAT and QSCAT on March 21, 2009 over Antarctica. Recall that QSCAT is at Ku-band, and ASCAT is at C-band. C-band typically has greater variability over land than Ku-band which explains why the ACAT V image is brighter over the land than the QSCAT images. On the other hand, over the ocean, the ASCAT V image is less bright than the QSCAT images. The fan beam design of ASCAT gives less azimuth angle diversity than QSCAT leading to a smaller variance for ASCAT over the ocean.

A few algorithms combine data from multiple instruments, including [18], [25]. These algorithms use both a scatterometer and a radiometer to map the ice extent. They are also gridded at the native resolutions of the instruments (12.5 km and worse). Currently, the algorithm presented by Brevik and Eastwood [18] is the only operational algorithm that uses ASCAT data. Ice maps with better resolution can be achieved with enhanced resolution SIR images [5]–[7].

This Section is outlined as follows: First, the NT algorithm is described. Following that, sea ice mapping with SIR images is presented, including a description of the different SIR images, and RL and Anderson's algorithms [5], [6].

2.3.1 NASA Team Algorithm

The NASA Team (NT) algorithm is used to estimate sea ice concentration from passive microwave instruments. The NT algorithm assumes the brightness temperature over the polar regions (excluding land) is a linear combination of open water and ice:

$$T_B = T_{BW}C_W + T_{BFY}C_{FY} + T_{BMY}C_{MY}, \qquad (2.4)$$

where C_W is the fraction of the area covered by water, T_{BW} is the brightness temperature contribution from ocean, C_{FY} is the fraction of the area covered by first year ice, T_{BFY} is the brightness temperature contribution from first year ice, C_{MY} is the fraction of the area covered by multiyear ice, and T_{BMY} is the brightness temperature contribution from multiyear ice. The total ice concentration is the sum of the first year and multiyear ice fractions: $C_i = C_{FY} + C_{MY}$.

The ice concentration calculation uses multiple channels and tie points to calculate the total ice concentration. The tie points are reference points for open water, first-year ice, and multiyear ice. For a detailed description on calculating the ice concentration see [3].

The NT algorithm produces reasonable estimates of the ice concentration. It has been modified to work with many radiometers. In addition, the algorithm has seen updates over the years to reduce errors. The main sources of error for the NT algorithm are weather effects, the presence of liquid water on ice (from melting snow and melt ponds), and new ice

15

having similar emission characteristics as open water [16]. Despite these shortcomings, the AMSR-E NT ice concentration maps are used as "truth" data to validate ice maps from the new algorithm.

2.3.2   Ice Mapping with SIR Images

As discussed in Section 2.2, the SIR algorithm enhances the resolution of scatterometer images. SIR images contain useful information for distinguishing sea ice from the ocean. A few ice extent algorithms use SIR images to map the ice extent [5]–[7]. This section describes the microwave characteristics of sea ice and ocean. Then, the properties of sea ice and ocean for each of the SIR images is described. Lastly, the Remund-Long (RL) algorithm [5] and Anderson's algorithm [6] are presented.

Ocean backscatter is dominated by surface scattering due to its high dielectric constant. When there is little wind, the ocean surface is smooth which means most of the incident radiation is reflected away from the scatterometer (specular scattering). On the other hand, higher winds roughens the surface of the ocean leading to higher backscatter values.

Sea ice has a different backscatter signature from the ocean. Surface scattering dominates for first-year and new ice, because the high brine content of first-year ice leads to a high dielectric constant [26]. First-year ice is typically rougher than the ocean surface leading to higher backscatter values. However, smooth first-year ice can have low backscatter values making it difficult to distinguish from the ocean. Multi-year ice is dominated by volume scattering leading to even higher backscatter values than first-year ice.

Under certain conditions, it is difficult to distinguish sea ice from the ocean using backscatter values. During the summer time, wet snow and melt ponds on the ice tend to reduce the backscatter making it difficult to distinguish the sea ice from the ocean. High winds increase the backscatter over the ocean which also reduces the contrast between sea ice and ocean.

The $\mathcal{A}$, $\mathcal{B}$, and V SIR images highlight different characteristics of the sea ice and ocean which allows the images to be used to distinguish sea ice and ocean. The $\mathcal{A}$ image represents the average $\sigma°$ over the imaging interval at 40° incidence angle. Sea ice has higher

16

backscatter values than the ocean under most conditions. However, high winds, smooth ice, wet snow and melt ponds can reduce the difference in backscatter between sea ice and ocean.

The $\mathcal{B}$ image shows the dependence of backscatter on incidence angle. Over incidence angles of interest ($\sim$30-60 degrees), the backscatter from a rough surface does not change much with incidence angle. On the other hand, a smooth surface has a wider range of backscatter as a function of incidence angle. Open water is generally smoother than sea ice, which makes it more dependent on the incidence angle [27]. For the $\mathcal{B}$ image from Figure 2.5(b), the ocean is typically further from zero (in both the positive and negative direction) than sea ice, because the ocean has greater dependence on incidence angle.

The V image is the variance of the reconstruction error which shows the variability of backscatter. Variations in backscatter are due to changes over time, azimuth angle, and incidence angle. The previous paragraph discussed why sea ice is less dependent on incidence angle. Sea ice is also relatively azimuth angle independent at C-band [28], while the ocean strongly depends on azimuth angle. Although, sea ice can change significantly in one day, the ocean surface is generally more dynamic, since it mainly depends on the near surface winds. Figure 2.6 shows that the ocean has higher values than the ice for a V image.

QSCAT has both vertical and horizontal polarization. The ratio of the horizontal to the vertical polarization is known as the co-polarization ratio (PR). The log of the ratio is equivalent to the difference in dB:

$$PR = \mathcal{A}_v - \mathcal{A}_h, \tag{2.5}$$

where $\mathcal{A}_v$ is the $\mathcal{A}$ image for vertical polarization (v-pol) and $\mathcal{A}_h$ is for horizontal polarization (h-pol). PR gives us information on both the incidence angle dependence and the polarization dependence. Over ocean, the v-pol values are typically higher than h-pol. Sea ice, on the other hand, shows no polarization bias. The many layers of sea ice are an inhomogeneous mixture of snow, brine pockets, air pockets, and the ice crystals. This randomness has the effect of depolarizing the incident wave. The PR images also exhibit an incidence angle dependence. Studies have shown that sea ice has greater isotropy in incidence angle

than open ocean [5], [10]. Due to these properties sea ice generally has a lower PR than the ocean.

RL Algorithm

The Remund-Long (RL) algorithm distinguishes the sea ice from the ocean using QSCAT SIR images. The RL algorithm was initially developed for the NASA Scatterometer (NSCAT), and was later updated for QSCAT [5], [29]. This thesis only describes the version for QSCAT.

The RL algorithm can be summarized into three steps:

1. Data fusion

2. Classification

3. Binary processing

The data fusion step consists of appropriately combining the relevant SIR images. For QSCAT the images used are: PR, $\mathcal{A}_h$, V_h, and V_v. The PR image is derived from $\mathcal{A}_h$ and $\mathcal{A}_v$ using (2.5). The images are normalized to have zero mean and unit variance. The feature vector is then weighted to give greater weight to the images with greater separability between sea ice and ocean. The feature vector with the weights used for the RL algorithm is: $[4PR, \mathcal{A}_h, V_v, V_h]$, with the greater weight given to PR because of its high contrast between ice and ocean.

The classification step uses an iterative maximum likelihood classifier. First, linear discrimination is used to produce an initial classification. From this classification, the mean vector, and covariance matrix for the ice and ocean distributions are computed. The maximum likelihood classifier is given by

$$C_{ML} = \arg\max_{C} P(\mathbf{x}|C), \tag{2.6}$$

where $\mathbf{x}$ is the feature vector, and C is the class (either ocean or sea ice). The RL algorithm assumes the sea ice and ocean distributions are jointly Gaussian. This simplifies Eq. (2.6)

to

$$C_{ML} = \arg\max_C \left\{ \frac{1}{(2\pi)^{n/2}|K_C|^{1/2}} e^{-\frac{1}{2}(\mathbf{x}-\boldsymbol{\mu}_C)^T K_c^{-1}(\mathbf{x}-\boldsymbol{\mu}_C)} \right\}, \qquad (2.7)$$

where $n = 4$ for QSCAT, K_C is the covariance matrix for the ice or ocean distribution, and $\boldsymbol{\mu}_C$ is the mean vector for the respective classes. Eq. (2.7) can further be simplified to

$$C_{ML} = \arg\min_C \left\{ \log|K_C| + (\mathbf{x} - \boldsymbol{\mu}_C)^T K_C^{-1}(\mathbf{x} - \boldsymbol{\mu}_C) \right\}. \qquad (2.8)$$

This maximum likelihood equation is performed iteratively with the number of iterations depending on the time of year.

The binary processing step is a series of standard digital image processing techniques used to reduce spurious misclassifications. This includes erosion, dilation, and region growing. In addition, a previous day's ice map can be used to constrain the growth/retreat of the sea ice. Although the binary processing reduces misclassifications, it also has the side effect of low pass filtering the ice edge. It also, filters out any polynyas within the sea ice. Despite these drawbacks, the ice maps produced from the RL algorithm have been successfully used in sea ice studies and other applications that need to know the ice extent. It was used operationally at JPL to retrieve ocean winds for the QSCAT mission.

Anderson's Algorithm

Anderson's algorithm [6] is related to the RL algorithm. It uses the same images to classify pixels as sea ice or ocean. However, instead of a maximum likelihood decision rule, it uses a Bayes decision rule of the form:

$$\phi(\mathbf{x}) = \begin{cases} \text{sea ice,} & \text{if } p(\mathbf{x}|\omega_1)L_{10} > p(\mathbf{x}|\omega_0)L_{01} \\ \text{ocean,} & \text{otherwise,} \end{cases} \qquad (2.9)$$

where $\mathbf{x}$ is the feature vector, ω_0 is the ocean class, ω_1 is the ice class, $p(\mathbf{x}|\omega_i)$ is the conditional probability density function (PDF) of the feature vector given the respective class, and L_{ij} are loss terms for incorrect decisions. The loss terms are created from the previous day's RL ice maps. The conditional PDF's are estimated from histograms. These histograms

are parameterized by a basis set of expected histograms. This algorithm includes several parameters that can be tuned to give better performance, and it also uses minimal binary processing compared to the RL algorithm. The disadvantage of using this algorithm is that it requires a training set and requires the RL ice maps as a starting point.

Chapter 3

Algorithm

In this chapter the new ice mapping algorithm is described. The new algorithm incorporates elements from both RL and Anderson's algorithms including an iterative pixel-based decision rule similar to both. In addition, digital image processing is used to reduce spurious misclassifications. The new algorithm differs from RL and Anderson in that it incorporates a prior and it uses a new type of image that shows azimuth modulation. In addition, data gaps in the images are classified using the previous day's ice map.

In summary, the new algorithm can be broken down into a series of steps:

1. Gather all relevant data (images and previous day's ice map).
2. Normalize images to have zero mean and unit variance.
3. Generate Prior Probability Maps (PPM) from previous day's ice map and thresholded **d** image.
4. Estimate conditional PDF of feature vector for both sea ice and ocean.
5. Classify each pixel using decision rule given by Eq. (3.1).
6. Update PPMs using current ice map.
7. Estimate conditional PDF using current ice map.
8. Digital image processing.
9. Repeat steps 5-8 (this is done 6 times).
10. Constrain ice map to maximum limit.
11. Median filter ice map.
12. Classify areas of no data using previous day's ice map.

The remainder of this chapter describes each step in the algorithm in detail. This chapter is outlined as follows: First, Section 3.1 presents the decision rule. Then, Section 3.2 discusses the images (features) used in the decision rule. Next, Section 3.3 discusses

estimation of the conditional PDF, and then, Section 3.4 describes the generation of the prior used by the algorithm. Finally, Section 3.5 discusses the iterations of the algorithm.

3.1 Decision Rule

The new algorithm uses a pixel-based Bayes decision rule of the form:

$$\phi(\mathbf{x}) = \begin{cases} \text{sea ice,} & \text{if } p(\mathbf{x}|\omega_1)P(\omega_1) > p(\mathbf{x}|\omega_0)P(\omega_0), \\ \text{ocean,} & \text{otherwise,} \end{cases} \tag{3.1}$$

where $\mathbf{x}$ is the feature vector, ω_0 is the ocean class, ω_1 is the ice class, $p(\mathbf{x}|\omega_i)$ is the conditional PDF of the feature vector given the respective class, and $P(\omega_i)$ is the prior probability for either sea ice or ocean. The decision rule is similar to Anderson's algorithm with the loss terms replaced by the prior probabilities [6]. The algorithm uses a slightly different feature vector than the Anderson or RL algorithm as described in the next section [5], [6].

3.2 Features

The feature vector $\mathbf{x}$ in Eq. (3.1) is composed of the pixel values from four images: $\mathcal{A}$, $\mathcal{B}$, V, and normalized difference ($\mathbf{d}$) images. The images have different ranges of values, so in order to combine them in an unbiased way, each image is normalized to have zero mean and unit variance [30]. Each image has different characteristics that aid in distinguishing the sea ice from the ocean. The sea ice and ocean characteristics for the $\mathcal{A}$, $\mathcal{B}$, and V images are discussed in Section 2.3.2.

A new image used in the decision rule is the normalized difference image ($\mathbf{d}$). The normalized difference is defined as:

$$d = \frac{|\sigma_F^\circ - \sigma_A^\circ|}{|\sigma_F^\circ + \sigma_A^\circ|}, \tag{3.2}$$

where σ_F° is the backscatter measurement from the fore antenna and σ_A° is the backscatter measurement of the aft antenna [10], [31]. ASCAT has six antennas with three on each side. The two antennas in the front are known as the fore antennas, and the two rear antennas are known as the aft antennas (see Figure 2.1). As ASCAT moves forward, a given spot on the

ground is illuminated by one of the fore antennas. A few seconds to minutes later, the same spot is illuminated by the corresponding aft antenna. For a single pass of the instrument, the fore and aft measurements over a given location are at the same incidence angle, but different azimuth angles. Thus, the normalized difference between the two measurements is a measure of the azimuth angle dependence of the illuminated area. The normalized difference is independent of incidence angle since both measurements are at the same incidence angle. In addition, it is independent of time, assuming that $\sigma°$ does not change in the time between the fore and aft measurements.

An image is generated from the normalized difference by projecting each d value onto the high resolution SIR grid. All of the d values that fall in a pixel are averaged. Figure 3.1 shows an example of a **d** image over Antarctica. Note that this image uses two days' of data. Two days are needed to achieve full coverage because the **d** images only use measurements from the fore and aft antennas, and not the mid antenna.

The feature vector used in the decision rule uses both one and two day images. ASCAT has better coverage over two days than a single day, so the two day images have smaller data gaps. In addition, two day images have more measurements leading to better estimates from the SIR algorithm. However, the ice edge can move several kilometers in a single day, which can make the ice edge less detectable in the two day images. Thus, both one and two day images are employed to optimize detection of ice extent.

3.3 Conditional PDF

Estimating the conditional PDF's, $p(\mathbf{x}|\omega_i)$ for each individual pixel is difficult. Thus, it is assumed that the pixel statistics are the same for each pixel. This assumption is also used in RL and Anderson's algorithm. However, in reality, the conditional PDF's for sea ice and ocean both depend on the location of the pixel. This spatial dependence is accounted for by the prior probabilities in Eq. (3.1).

A few approaches for estimating the conditional PDF's are considered here. One approach is to assume the PDF's are Gaussian. Only the mean vector and covariance matrix need to be estimated with this approach which is used by the RL algorithm [5]. Another
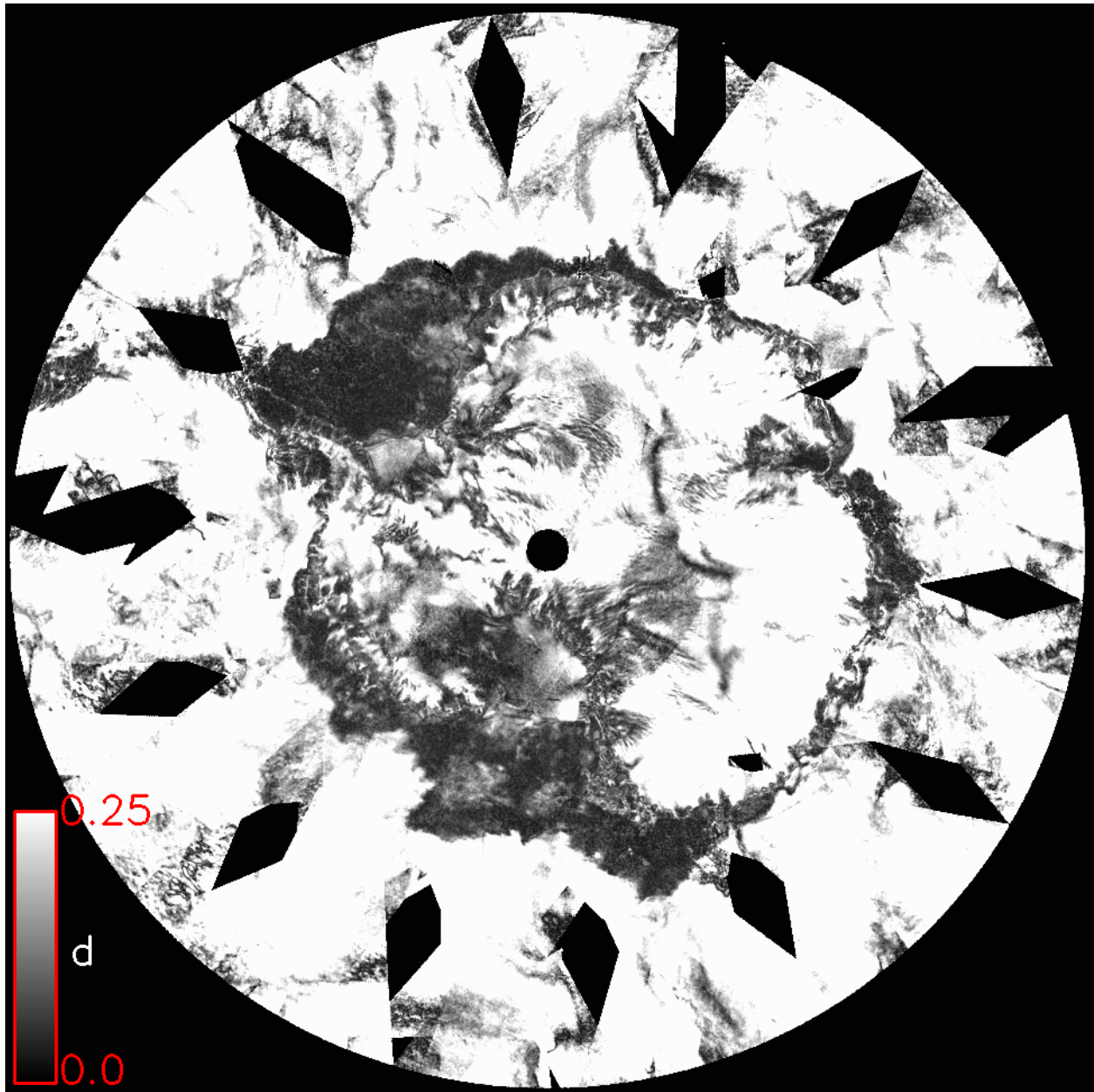
Figure 3.1: ASCAT **d** image over Antarctica using measurements from March 21-22, 2009.

approach is to use histograms to estimate the conditional PDF's which is used by Anderson [6]. Histograms are more versatile at modeling the underlying PDF; however, they require more memory than the Gaussian approach. I denote using Gaussian PDF's as the Gaussian method and using histograms as the histogram method. Next, the advantages of both methods is discussed.

3.3.1 Comparing Conditional PDF's

Ice maps are generated using both the histogram and Gaussian methods. The median filter used in step 11 is assumed to be square for simplicity. Since both dimensions of the filter are equal, one value can be considered for the size. Several values (M_f) are considered for the size of the median filter used in step 11 of the algorithm. The value of M_f has the most significant impact on the final output, especially when using Gaussian PDF's.

Figures 3.2 and 3.3 plot the percentage error in area between the new ice maps and the AMSR-E NT 15% ice concentration maps. The Gaussian method performs significantly better as M_f increases in the Antarctic. On the other hand, the histogram method is not as dependent on the value of M_f, but tends to have greater error with increasing M_f. These plots are thus not conclusive on which method should be used. The histogram method performs better for smaller M_f, but the Gaussian method has the best overall results (when $M_f = 30$ for the Antarctic and $M_f = 20$ for the Arctic).

The plots from Figures 3.2 and 3.3 only show the overall error. It is helpful to do a more in-depth examination of the types of errors present in the ice maps. Two types of errors can occur: a pixel classified as sea ice that is actually ocean (false alarm), and a pixel classified as ocean that is actually sea ice (missed detection).

Figures 5.5(a) and 5.5(b) show the total area of false alarms for each month for different values of M_f. The Gaussian method has much fewer false alarms. Notice that false alarms in the Antarctic are not significantly affected by M_f. However, the Arctic is affected by M_f, with a smaller M_f giving better results. This implies that a small median filter is best for minimizing false alarms.
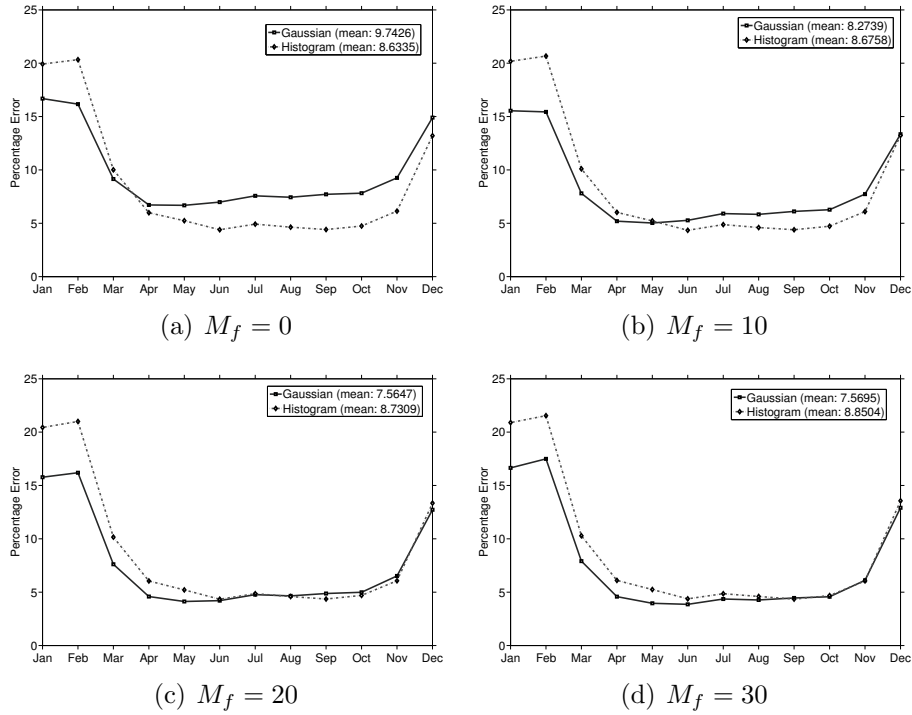
Figure 3.2: Percentage error in area for each month of the year in 2008 over Antarctica for different median filter sizes and for both the Gaussian and histogram methods.
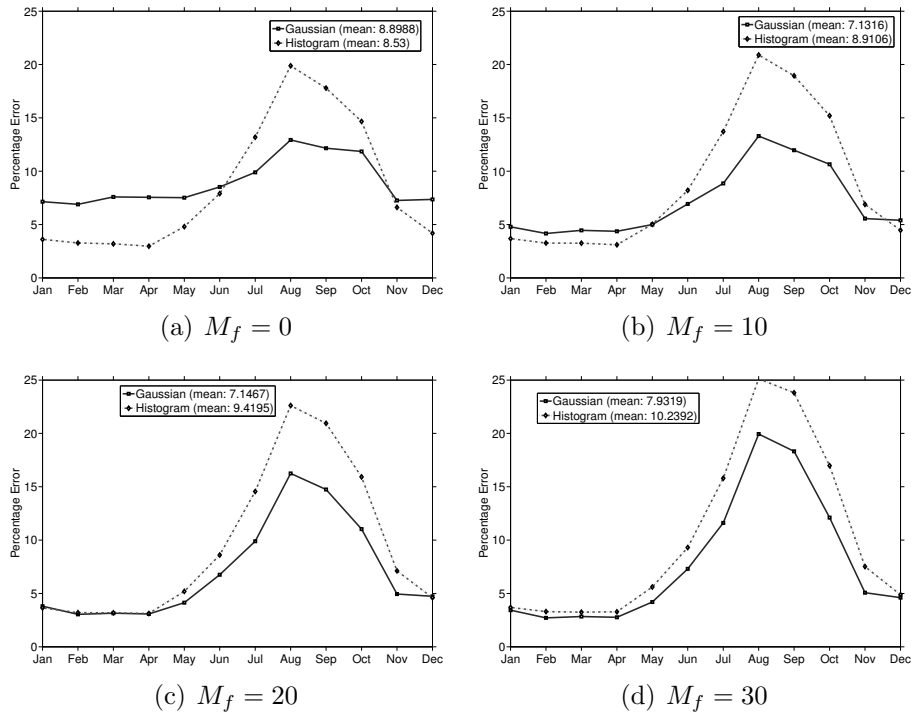

Figure 3.3: Percentage error in area for each month of the year in 2008 over the Arctic for different median filter sizes and for both the Gaussian and histogram methods.
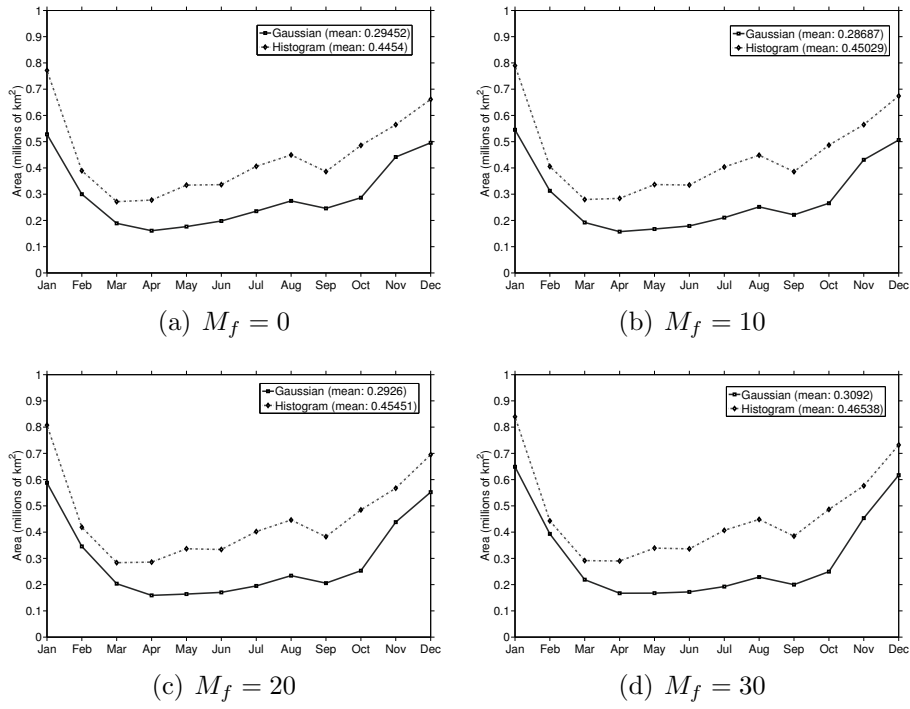
Figure 3.4: Total area of false alarms for each month of the year in 2008 over Antarctica for different median filter sizes and for both the Gaussian and histogram methods.
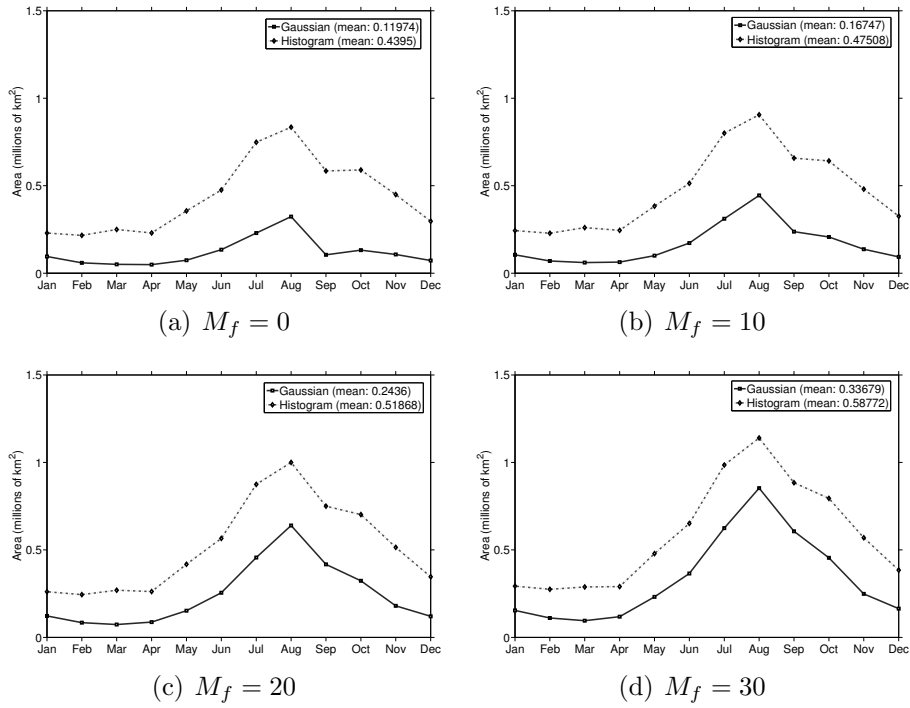

Figure 3.5: Total area of false alarms for each month of the year in 2008 over the Arctic for different median filter sizes and for both the Gaussian and histogram methods.

Missed detections are pixels classified as ocean that are actually sea ice. Figures 5.4(a) and 5.4(b) show the total area in missed detections for each month for different values of M_f. For most months, the histogram method has fewer missed detections. Note that the histogram method is not particularly sensitive to the value of M_f; however, the Gaussian method is sensitive with a larger M_f giving fewer missed detections.
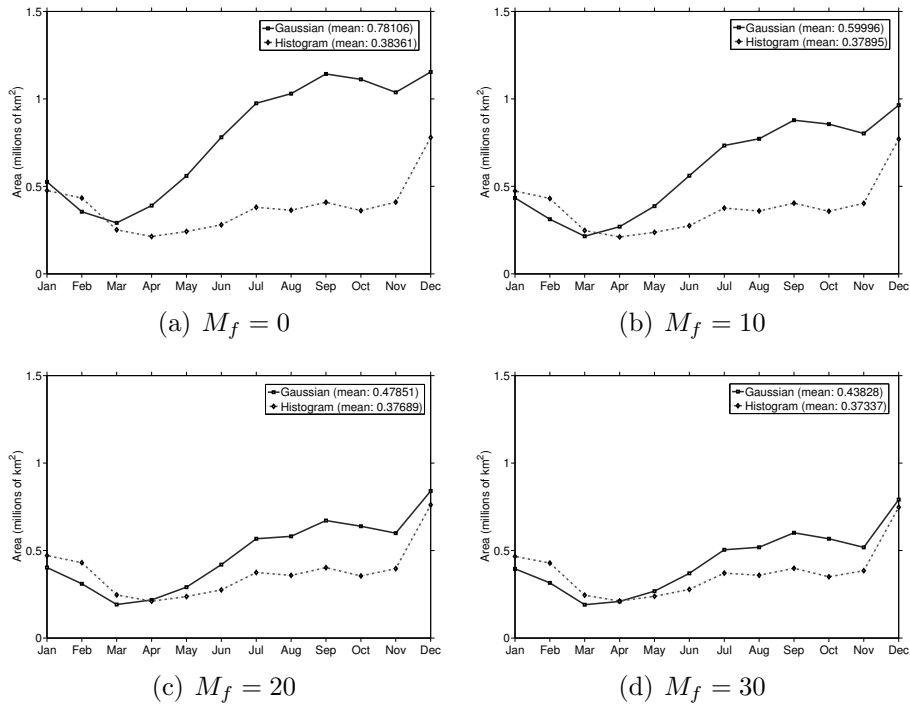

Figure 3.6: Total area of missed detections for each month of the year in 2008 over Antarctica for different median filter sizes and for both the Gaussian and histogram methods.

Generally speaking, the Gaussian method has fewer false alarms, and the histogram method has fewer missed detections. These observations suggest that combining both methods in the new algorithm can achieve the best overall results.
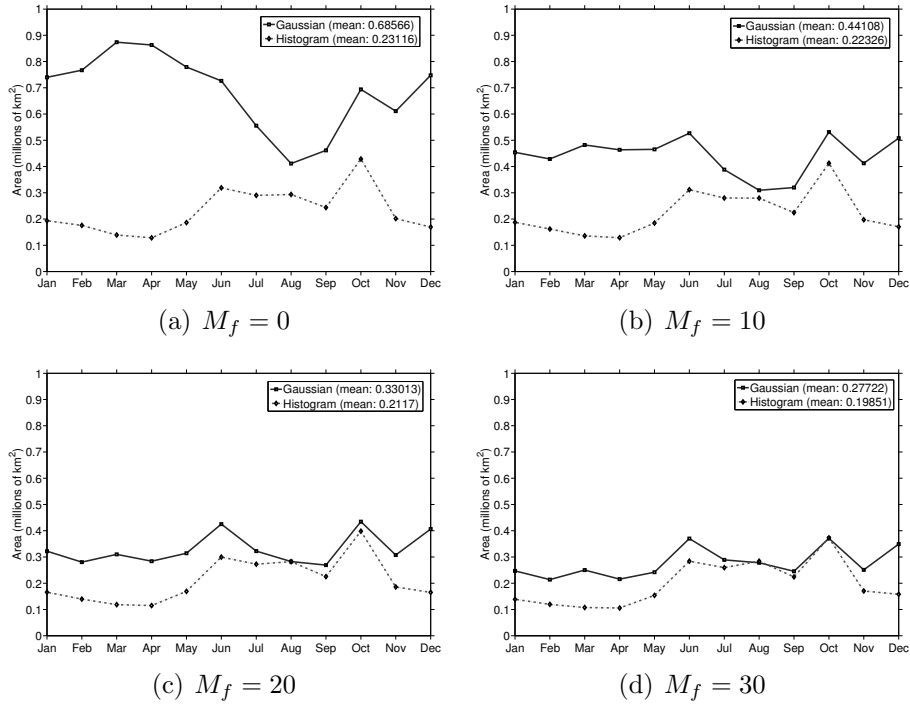
Figure 3.7: Total area of missed detections for each month of the year in 2008 over the Arctic for different median filter sizes and for both the Gaussian and histogram methods.

3.4 Prior

The prior probabilities in Eq. (3.1) enable the decision rule to have a spatial dependence and constrain the growth/retreat of the ice from day to day. A prior probability is assigned to each pixel in the images. The resulting image is denoted a Prior Probability Map (PPM). The PPM uses an ice map from the previous day and a normalized difference image. If an ice map from the previous day does not exist, then the next available previous day is used up to five days before.

Equation 3.1 includes a prior probability for both sea ice and ocean. The sea ice PPM is generated first, and the ocean PPM is derived from the sea ice PPM.

To generate a sea ice PPM, first, a mask is created using the previous day's ice map. This is depicted in Figure 3.8(a). Note that both land and sea ice pixels are white in the mask. Next, a Gaussian filter is applied to the mask. The algorithm is not particularly sensitive to the exact values used for the kernel size and standard deviation of the Gaussian

filter. The standard deviation, σ_i, and size of the kernel represent the uncertainty of the current day's ice mask when compared with the previous day's mask.

For the next step, the PPM is given a maximum and minimum value. The maximum and minimum values constrain the PPM to have a finite probability for both sea ice and ocean. I chose a maximum value of 0.95 and minimum value of 0.05. This minimum value is used by Anderson for the loss terms [6]. Anderson used a maximum value of one; however, the maximum value of 0.95 employed in the new algorithm is used because it represents a probability. A value of 1 would mean that no decision is made. After setting the limits on the sea ice PPM, the ocean PPM is found from: $P(\omega_0) = 1 - P(\omega_1)$, since there are only two classes. Figure 3.8(b) illustrates an example of a filtered mask with the maximum and minimum values.
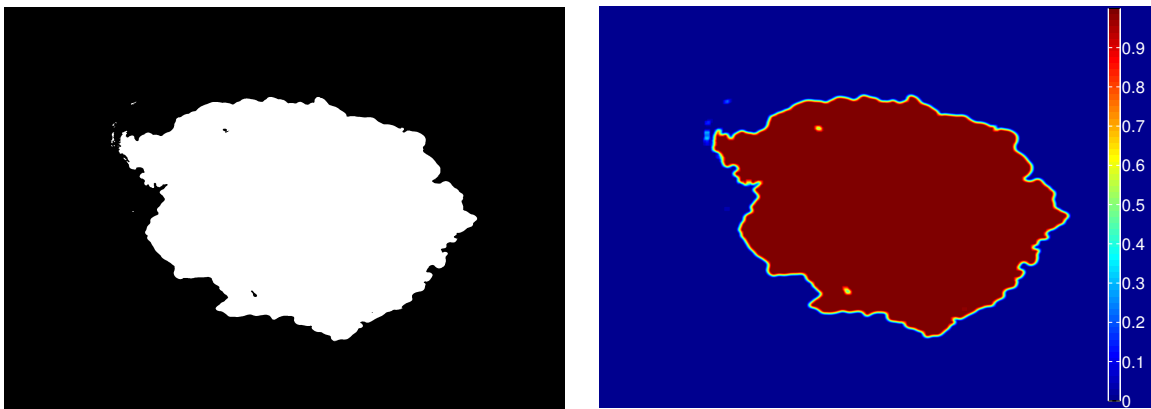
(a) Initial mask where land and sea ice are white. (b) After filtering with a Gaussian kernel and setting maximum and minimum values

Figure 3.8: Steps showing the sea ice PPM using the previous day's ice map from March 21 2009 in Antarctica.

Occasionally, a previous day's ice map is not available or does not accurately map the ice extent. Thus, the algorithm must have the ability to recover from a bad or missing previous day's ice map. Otherwise, a bad ice map can produce errors that propagate for several days. To overcome this issue, a thresholded **d** image is employed because it has high contrast between ice and ocean.

The **d** PPM is created from a thresholded **d** image. To make the **d** PPM, first, all non-land pixels above a threshold are given a value of 1. In addition, all land pixels are given a value of 1. An example of a thresholded **d** image is shown in Figure 3.9(a). For next step in making the **d** PPM, a median filter is applied to the thresholded image as shown in Figure 3.9(b). This step reduces the speckle seen in Figure 3.9(a). Lastly, region growing is applied to the image to get rid of disjoint pieces as shown in Figure 3.9(c). The resulting binary mask is a reasonable initial estimate of the ice extent. A prior is created from this binary mask in the same way as the previous day's PPM with the Gaussian filter and maximum and minimum values. An example of a sea ice PPM using a **d** image is shown in Figure 3.9(d).

In order to determine the optimal threshold and median filter size (M_d) for the **d** PPM, several values for the median filter size and threshold are considered. Appendix B evaluates the effects of different values for M_d and the threshold when the **d** PPM is compared to the ASMR-E 15% ice concentration maps. A threshold of 0.15 minimizes the percentage error in area in the Antarctic, and a threshold of 0.125 minimizes the error in the Arctic. Figure 3.10 shows the percentage error in area using a threshold of 0.15 for the Antarctic, and 0.125 for the Arctic. Several values for M_d are plotted in the figures using these threshold values. In the Arctic, $M_d = 15$ provides the best results, while in the Antarctic, $M_d = 20$ provides the best results.

The initial PPM used by the algorithm is found from a weighted average between the PPM from the previous day's ice map, and the PPM from the **d** image. It is expected that the previous day's PPM is usually a more accurate representation of the sea ice for the current day than the **d** PPM. However, the **d** PPM is given greater weight in the average, because an inaccurate ice map can produce errors which propagate through several days. By giving the **d** image PPM more weight, these errors can be reduced with the trade-off of a potentially less accurate initial PPM.

With each iteration, the PPM is updated with the current ice map. Anderson uses a similar update procedure for the loss maps [6]. Initially, a mask is created with the current ice map where ice and land pixels are given a value of one. In addition, the areas that have
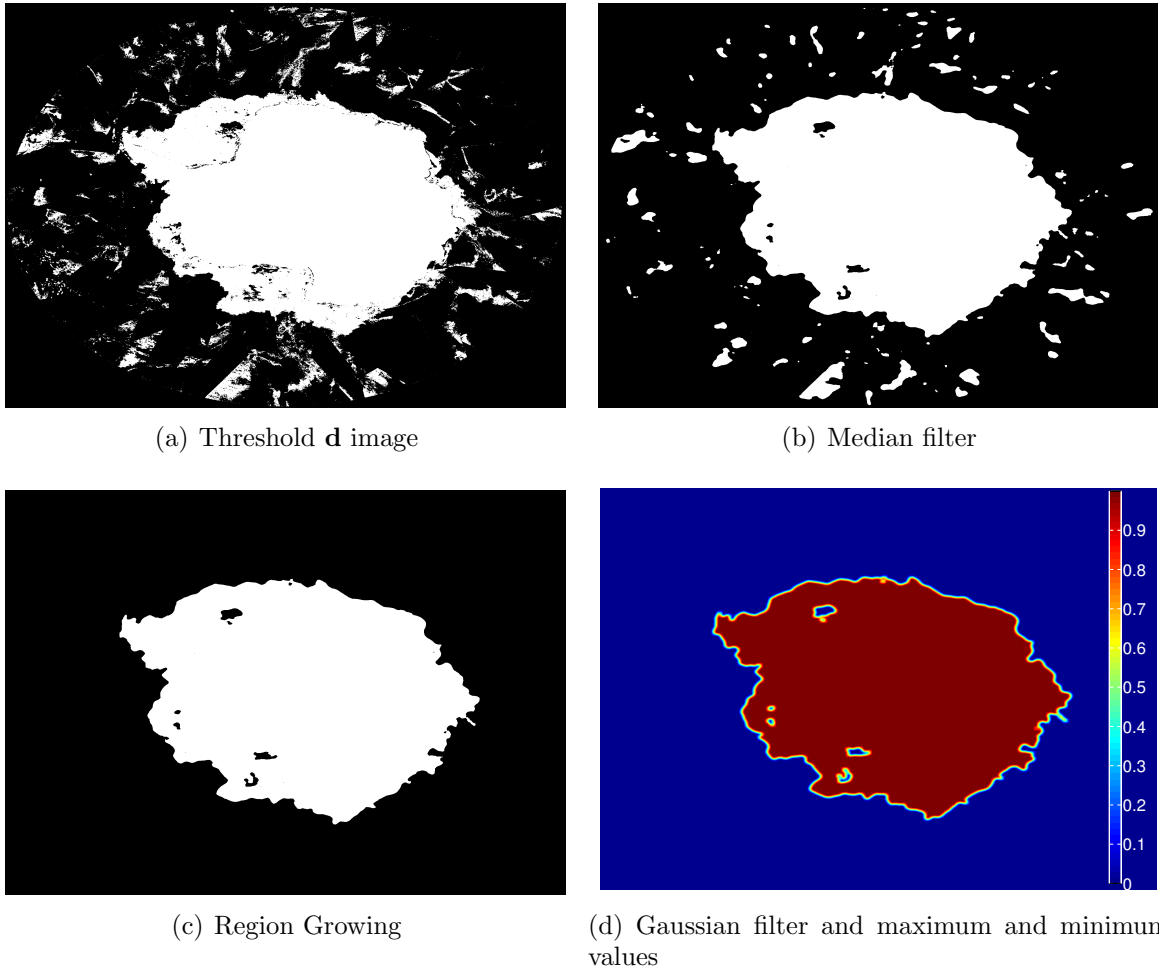
(a) Threshold **d** image

(b) Median filter

(c) Region Growing

(d) Gaussian filter and maximum and minimum values

Figure 3.9: Steps to create the sea ice PPM using the thresholded **d** image on March 21, 2009 over Antarctica.
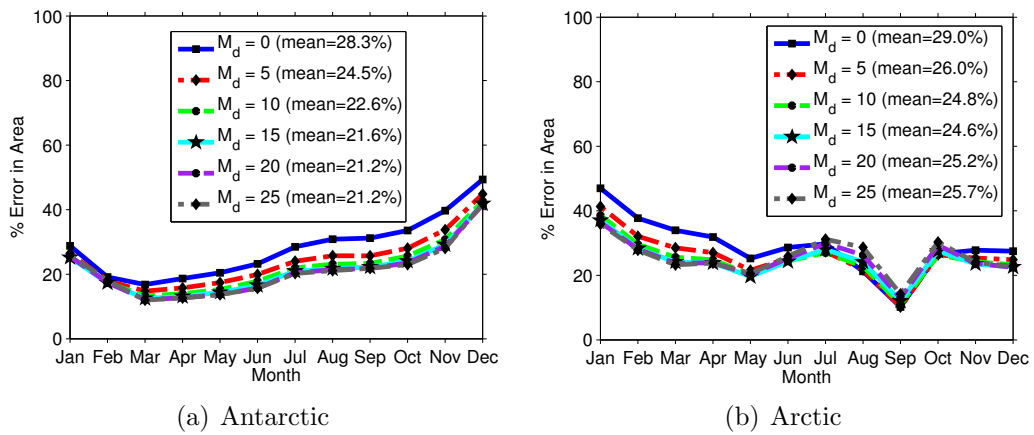

(a) Antarctic

(b) Arctic

Figure 3.10: Percentage error in area for the thresholded **d** image using a threshold of 0.15 in Antarctica and 0.125 in the Arctic. The thresholded **d** images are compared to the AMSR-E NT 15% ice concentration maps for various filter sizes.

not been classified due to missing data are also given a value of one where the previous day's ice map said there was ice. This avoids discontinuities that exist from missing data (i.e. the black diamonds). Then, a Gaussian filter is applied to this image, but this time with a smaller standard deviation than the previous iteration. The standard deviation linearly decreases to 0 with each iteration. The idea is that with each iteration, the mask converges to the actual ice extent. For the final step in updating the prior, a weighted average is performed with the filtered image and the PPM from the previous iteration:

$$P^t(\omega_1) = \alpha \hat{P}^t(\omega_1) + (1 - \alpha)P^{t-1}(\omega_1), \tag{3.3}$$

where $P^{t-1}(\omega_1)$ is the PPM from the previous iteration, $\hat{P}^t(\omega_1)$ is the filtered image from the current ice map, and $\alpha \in [0, 1]$ is a "forgetting" factor that adjusts how much the previous iteration's PPM is used. Different values of α are considered in the next chapter. Lastly, the PPM is constrained to the same min/max values as described previously in this section.

3.5   Iterations

The optimal combination of images and iterations is difficult to find. However, the algorithm is not particularly sensitive to the specific combination. In addition, the ice map does not change significantly after only a few iterations. Thus, the algorithm is broken down into two sections that each use a few iterations.

The first section uses Gaussian PDF's with three iterations. As described in Section 3.3 the Gaussian method has fewer false alarms, but more missed detections. A false alarm on the ice edge can be difficult to remove. Thus, using Gaussian PDF's gives a good idea of the ice edge. However, there may be an increase in the missed detections, especially within the ice.

Although the choice of three iterations at this stage is somewhat arbitrary, it is again noted that the ice map has been observed to change only slightly when using more iterations. The choice of which images to use for each iteration is also somewhat arbitrary. It is noted that two day images provide better coverage and are less susceptible to noise; however, the ice

edge is not as well defined for two day images, especially the **d** images. Thus, a combination of one and two day images are employed.

For the first iteration, one day $\mathcal{A}$, $\mathcal{B}$ and V images are employed. The second iteration uses two day versions of these images, and the third iteration uses the one day images used in the first iteration. This particular combination is chosen because the goal of the algorithm is to produce an ice map that approximately represents the current day's ice extent. Thus, the one day images are used for the first and last iteration.

After the first section of the algorithm, a few digital image processing techniques are employed. Recall the first section of the algorithm uses Gaussian PDF's which gives a good representation of the ice edge. However, there are a still a number of missed detections. These missed detections typically appear as holes within the sea ice. These holes are filled using morphological reconstruction [32]. The resulting map is then median filtered to reduce spurious misclassifications.

The second section of the algorithm starts after the hole filling and median filtering. This section of the algorithm uses histograms to estimate the conditional PDF. As shown in Section 3.3 the histogram method typically has fewer missed detections than the Gaussian method. Thus, it is expected that this method can more accurately detect polynyas within the ice. Only pixels classified as ice from the first section are classified in the second section. This is because histograms do not perform as well as the Gaussian method when classifying in the open ocean (more false alarms). This section uses the same number of iterations as the first. In addition, the same images are used for each iteration.

A few final steps are performed after all of the iterations. Steps 10 and 11 are meant to reduce spurious errors. Two types of errors are present in the ice map: ocean classified as sea ice (false alarm) and sea ice classified as ocean (missed detection). To reduce false alarms, we place a constraint on how much the ice can grow in a single day. A dilated version of the previous day's ice map gives a maximum limit that we allow the ice to grow in a single day. A value of 20 is used for the dilation factor which is a generous value. It is noted that a bad previous day's ice map can produce errors. However, due to the large dilation factor, these errors only propagate for a few days. A median filter reduces speckle noise which helps
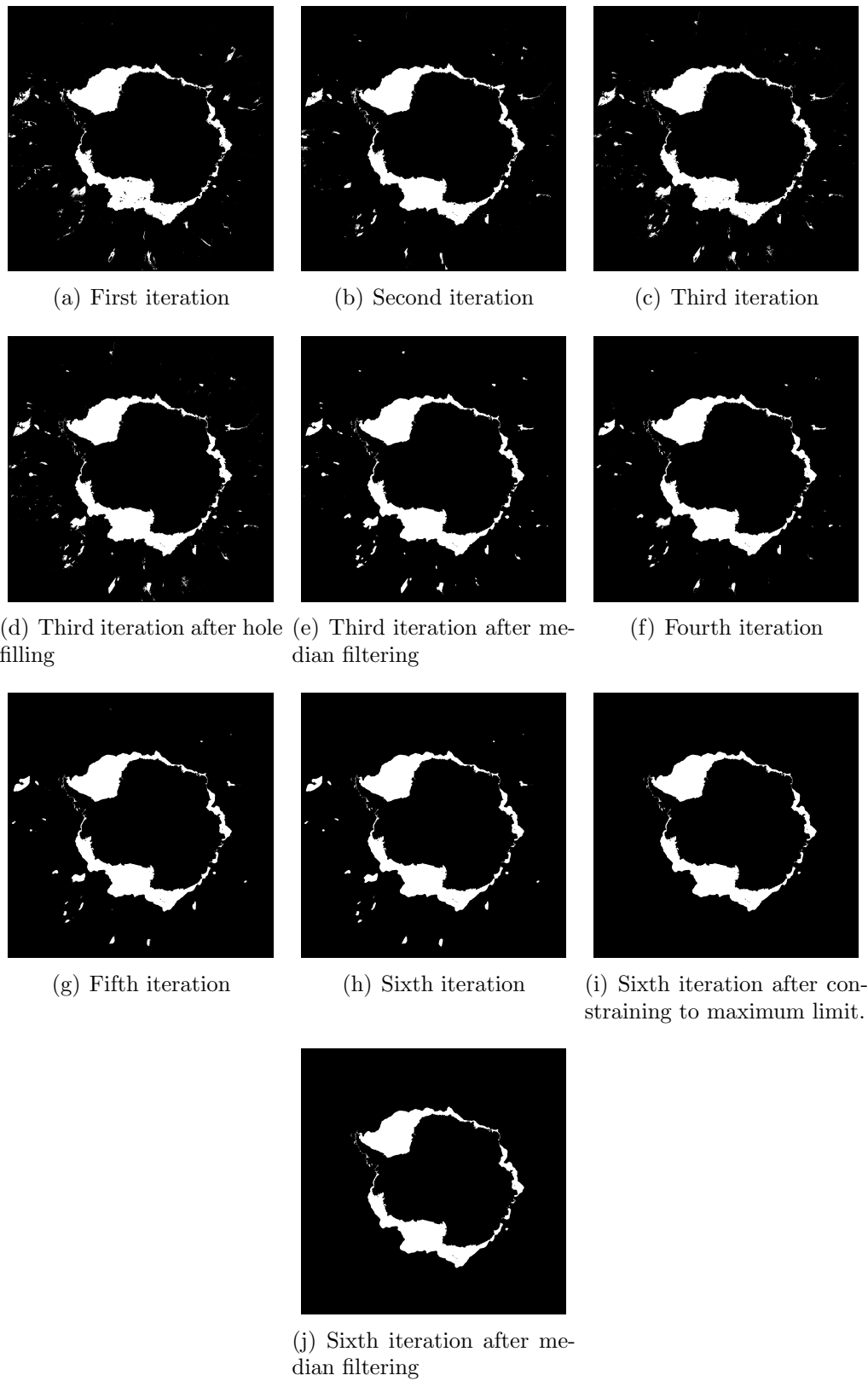
(a) First iteration

(b) Second iteration

(c) Third iteration

(d) Third iteration after hole filling

(e) Third iteration after median filtering

(f) Fourth iteration

(g) Fifth iteration

(h) Sixth iteration

(i) Sixth iteration after constraining to maximum limit.

(j) Sixth iteration after median filtering

Figure 3.11: What the ice map looks like after each iteration on March 21, 2009 in Antarctica.

eliminate missed detections and false alarms while preserving the edge. The final step of the algorithm fills in areas where there is no data with the previous day's classification, to give a spatially consistent ice map. Figure 3.11 shows what the ice map estimate looks like at each iteration for each section of the algorithm.

Chapter 4

Algorithm Tuning

This chapter considers several values for the tuning parameters introduced in the previous chapter. The goal is to minimize the percentage error in area with the AMSR-E NT 15% ice concentration maps. The NT maps are used because they are an acceptable source frequently used for comparison to verify other ice mapping algorithms [5]–[8]. In addition, the 15% concentration is typically used as the ice edge in literature [16].

The chapter is outlined as follows: First, Section 4.1 discusses the percentage error in area with several values for certain parameters. Then, Section 4.2 presents the parameters that give the best overall results.

4.1 Percentage Error in Area

Ice maps are created from ASCAT for all of 2008 for both the Arctic and the Antarctic using different values of the tuning parameters. An exhaustive study of possible values for the parameters is not performed. However as described below, several case studies are performed using different values for various parameters.

Table 4.1 lists the images and conditional PDF method used for each iteration. Some parameters are held constant for all of the case studies. It is left to future work to try different values for these fixed values; however, it is noted that the algorithm is not particularly sensitive to the exact values used for the chosen parameters. Table 4.2 lists the parameters held constant for all case studies.

The parameters whose values are varied in this case study are: M_1 - the median filter size after the third iteration, M_f - the value of the final median filter, α - the forgetting factor for updating the PPMs, and σ_i - the initial standard deviation for the Gaussian kernel.

Table 4.1: Images Used For Each Iteration.

| Iteration | Number of Days | | | | PDF Method |
	$\mathcal{A}$	$\mathcal{B}$	V	**d**	
1	1	1	1	-	Gaussian
2	2	2	2	-	Gaussian
3	1	1	1	-	Gaussian
4	1	1	1	-	Histogram
5	2	2	2	-	Histogram
6	1	1	1	-	Histogram

Table 4.2: Constant Parameters

Parameter	Value
iterations	6
prior minimum value	0.05
prior maximum value	0.95
maximum limit dilation factor	20
previous day's PPM weight	0.4
d PPM weight	0.6
kernel size for PPM Gaussian filter	20 by 20

Table 4.3 lists the various values used for each of these parameters. The range of values used for each of the parameters provided a compromise between computation time and covering values that provide reasonable results.

Table 4.3: Varied Parameters

| Parameter	Values
M_1	0, 10, 20
M_f	0, 10, 20, 30
α	0.0, 0.2, 0.4, 0.6, 0.8, 1.0
σ_i	0, 10, 20, 30, 40

(a) Antarctic   (b) Arctic
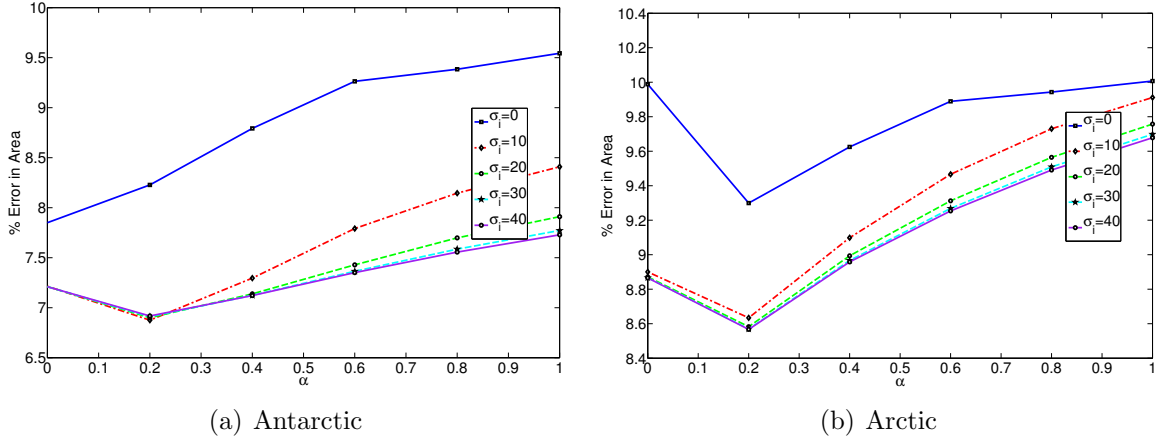
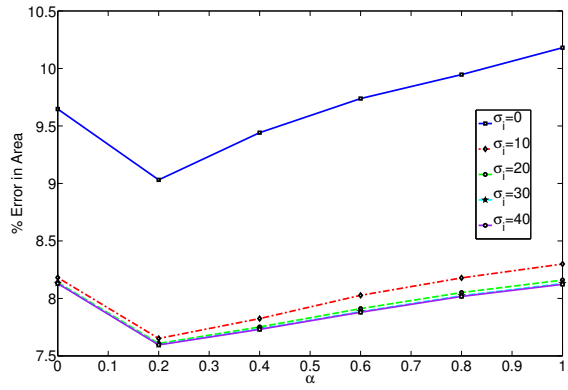**Figure 4.1:** Percentage error in area with $M_1 = 0$ and $M_f = 0$.

(a) Antarctic   (b) Arctic
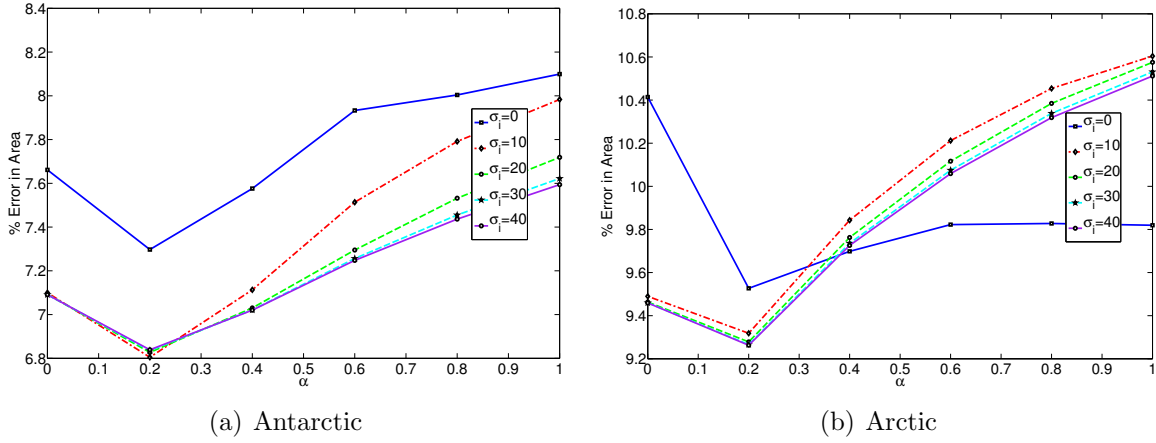
Figure 4.2: Percentage error in area with $M_1 = 0$ and $M_f = 10$.

Figures 4.1-4.4 show the percentage error in area for various values of α, σ_i, and M_f when $M_1 = 0$. Increasing σ_i generally gave better results, and $\alpha = 0.2$ generally minimized the error. This is because $\sigma_i = 0$ means there is no Gaussian filter. In the Arctic, the minimum error is 8.57% and occurs when $\sigma_i = 40$, $\alpha = 0.2$ and $M_f = 0$. In the Antarctic, the minimum error is 6.80% and occurs when $\sigma_i = 10$, $\alpha = 0.2$, and $M_f = 10$.

Figures 4.5-4.8 show the percentage error in area for various values of α, σ_i, and M_f when $M_1 = 10$. The results are similar to the Figures 4.1-4.4 when $M_1 = 0$. In this case,
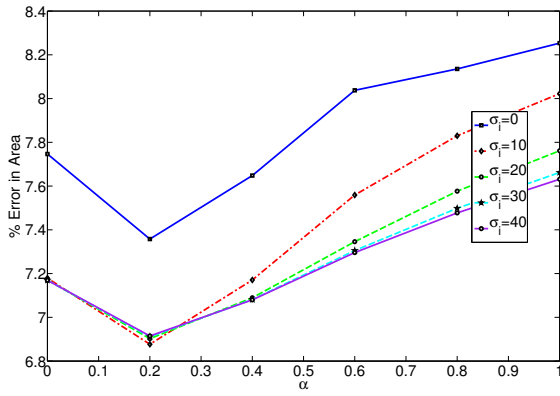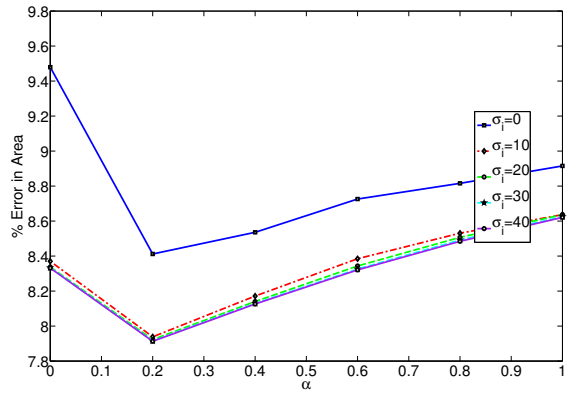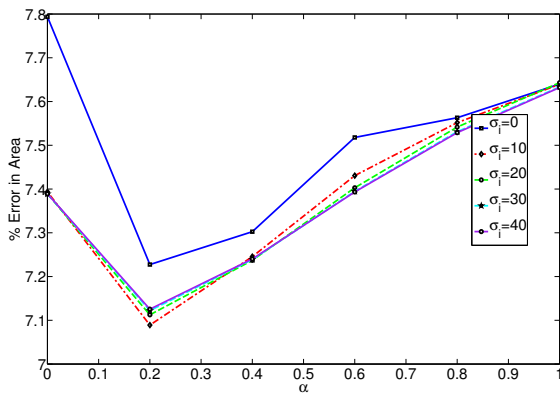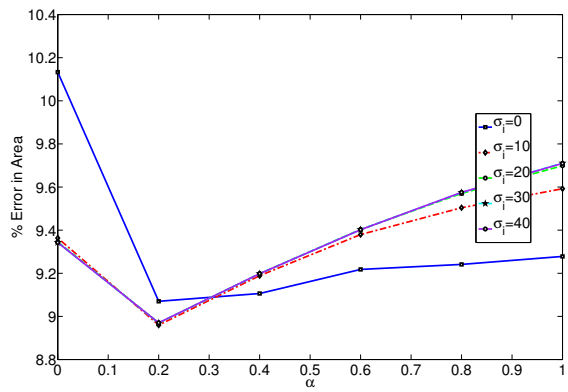
(a) Antarctic   (b) Arctic
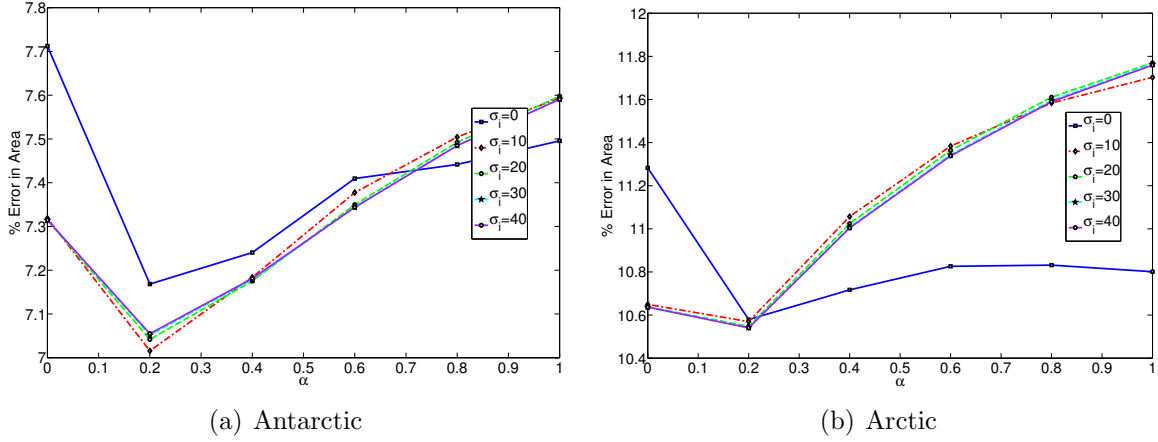
Figure 4.3: Percentage error in area with $M_1 = 0$ and $M_f = 20$.

(a) Antarctic   (b) Arctic
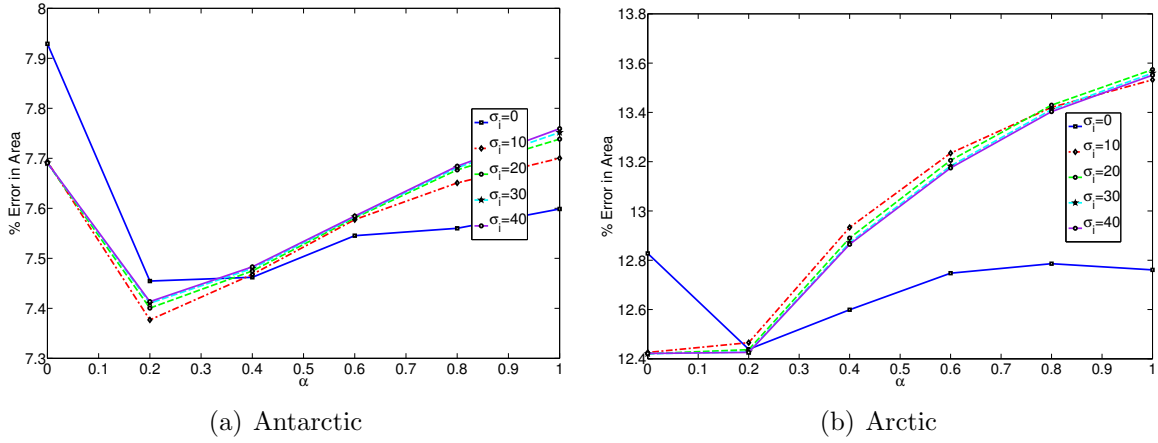
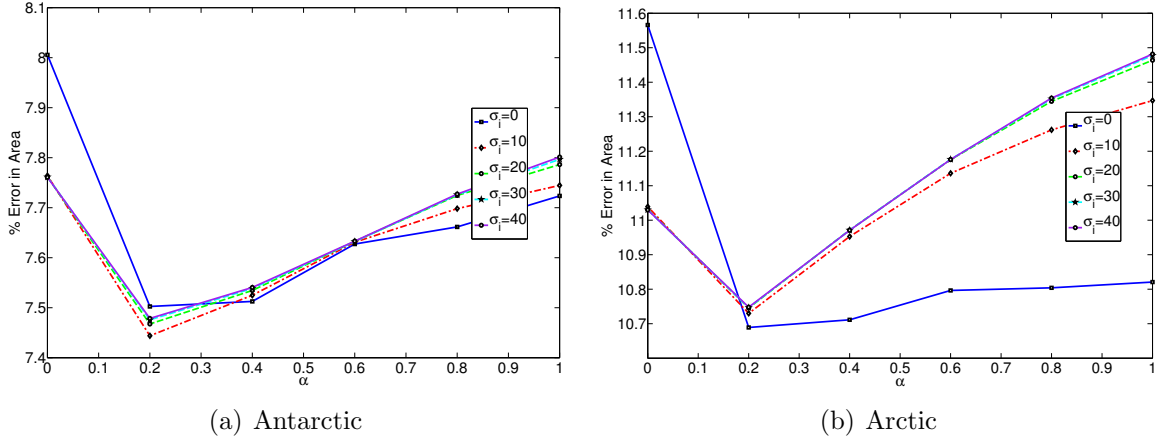**Figure 4.4:** Percentage error in area with $M_1 = 0$ and $M_f = 30$.

the minimum error in the Arctic is 7.60% and occurs when $\sigma_i = 40$, $\alpha = 0.2$, and $M_f = 0$ and the minimum error in the Antarctic is 6.85% and occurs when $\sigma_i = 10$, $\alpha = 0.2$, and $M_f = 0$. The error in the Arctic is slightly better than when $M_1 = 0$, while the error is slightly worse for the Antarctic.

Figures 4.9-4.12 show the percentage error in area for various values of α, σ_i, and M_f when $M_1 = 20$. The minimum error in the Arctic is 8.24% and occurs when $\sigma_i = 40$, $\alpha = 0.2$, and $M_f = 10$. The minimum error in the Antarctic is 6.93% and occurs when
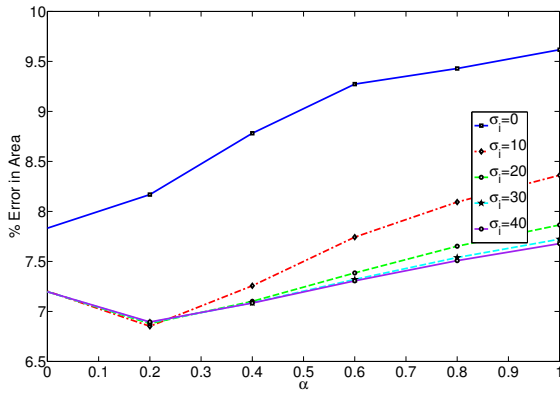
(a) Antarctic　　　　　　　　(b) Arctic

Figure 4.5: Percentage error in area with $M_1 = 10$ and $M_f = 0$.

(a) Antarctic　　　　　　　　(b) Arctic

Figure 4.6: Percentage error in area with $M_1 = 10$ and $M_f = 10$.

(a) Antarctic　　　　　　　　(b) Arctic

Figure 4.7: Percentage error in area with $M_1 = 10$ and $M_f = 20$.

(a) Antarctic

(b) Arctic

Figure 4.8: Percentage error in area with $M_1 = 10$ and $M_f = 30$.

(a) Antarctic
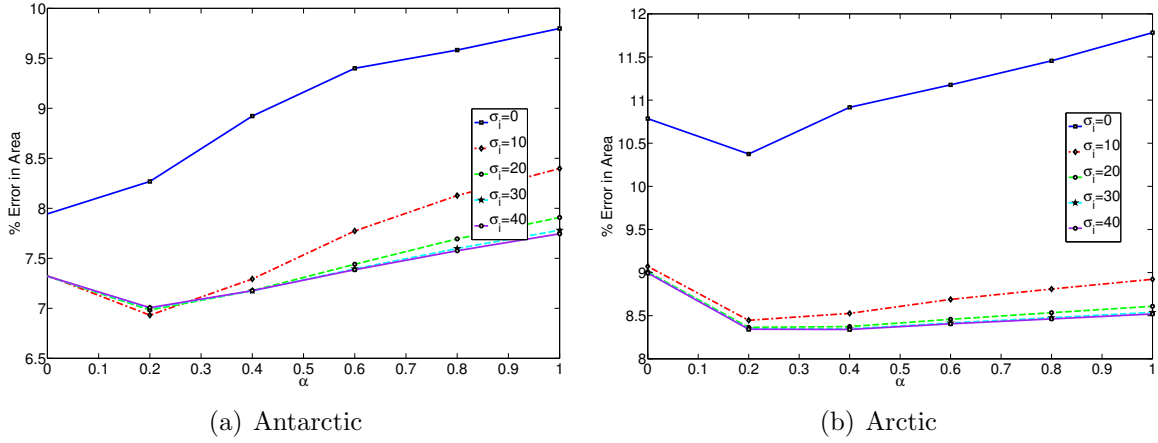
(b) Arctic

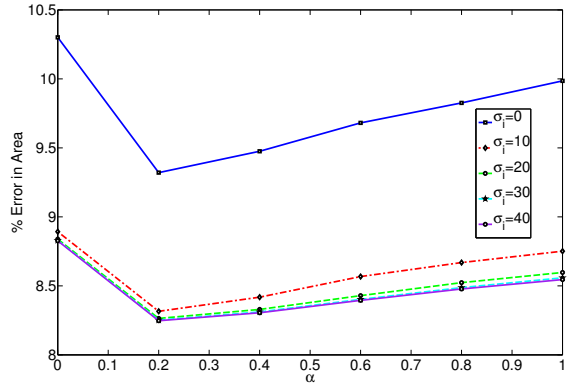**Figure 4.9:** Percentage error in area with $M_1 = 20$ and $M_f = 0$.

$\sigma_i = 10$, $\alpha = 0.2$, and $M_f = 0$. The error in the Antarctic increased slightly as M_1 increased. On the other hand, the error in the Arctic is minimized when $M_1 = 1$.

4.2   Parameter Values

Based on the results considered, Tables 4.4 and 4.5 list the parameters that give the lowest percentage error in area with the NT 15% ice concentration maps. For both regions, $\alpha = 0.2$ gave the best results. All the other parameters are slightly different for the two
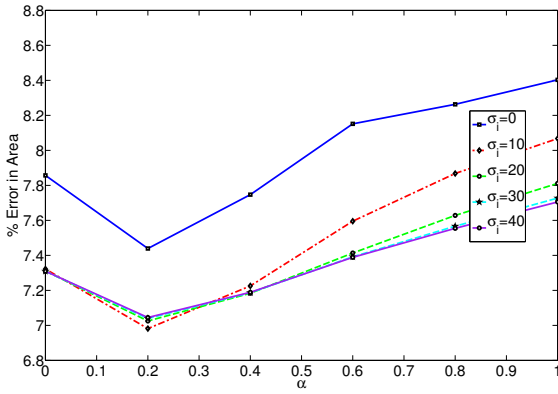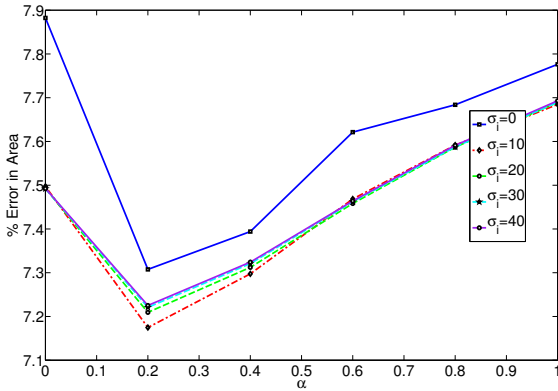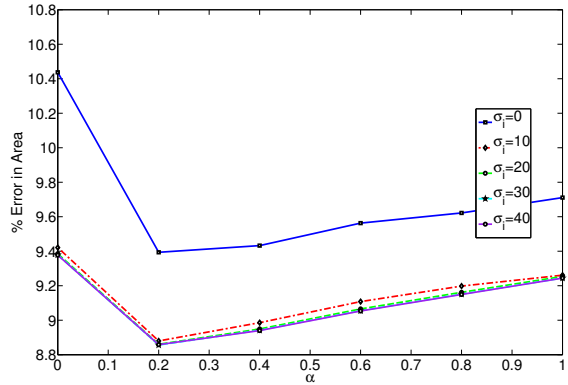
(a) Antarctic   (b) Arctic

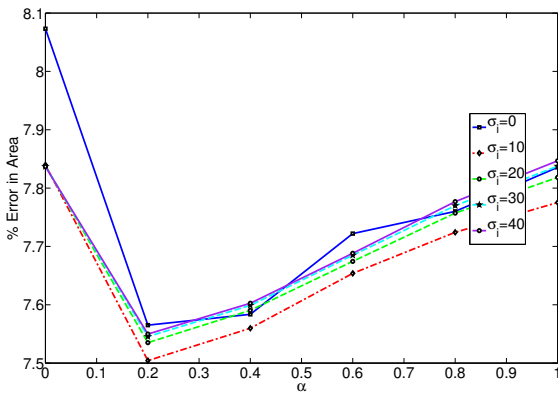**Figure 4.10:** Percentage error in area with $M_1 = 20$ and $M_f = 10$.

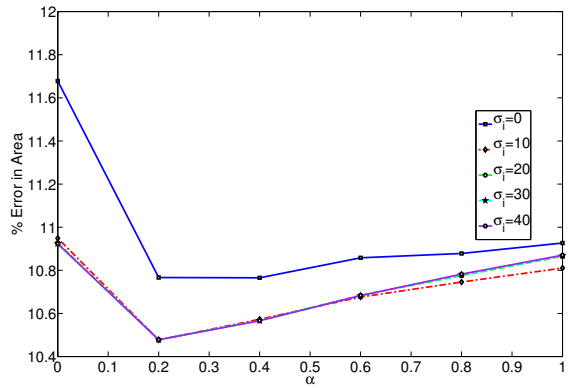(a) Antarctic   (b) Arctic

Figure 4.11: Percentage error in area with $M_1 = 20$ and $M_f = 20$.

(a) Antarctic   (b) Arctic

Figure 4.12: Percentage error in area with $M_1 = 20$ and $M_f = 30$.

regions. These differences are due to the differences in geographies in the polar regions as well as the differences in the characteristics in the sea ice.

Table 4.4: Antarctic Parameters

Parameter	Description	Value
M_1	Intermediate median filter	0
M_f	Final median filter	10
σ_i	Standard deviation of Gaussian kernel	10
α	Forgetting factor	0.2

Table 4.5: Arctic Parameters

Parameter	Description	Value
M_1	Intermediate median filter	10
M_f	Final median filter	0
σ_i	Standard deviation of Gaussian kernel	40
α	Forgetting factor	0.2

An example ice map for the Arctic and the Antarctic on March 21, 2009 is shown in Figure 4.13. These ice maps are made using the parameters listed in Tables 4.1, 4.2, 4.4, and 4.5. The parameters listed in Tables 4.4 and 4.5 consistently produce ice maps that agree well with the AMSR-E 15% ice maps.
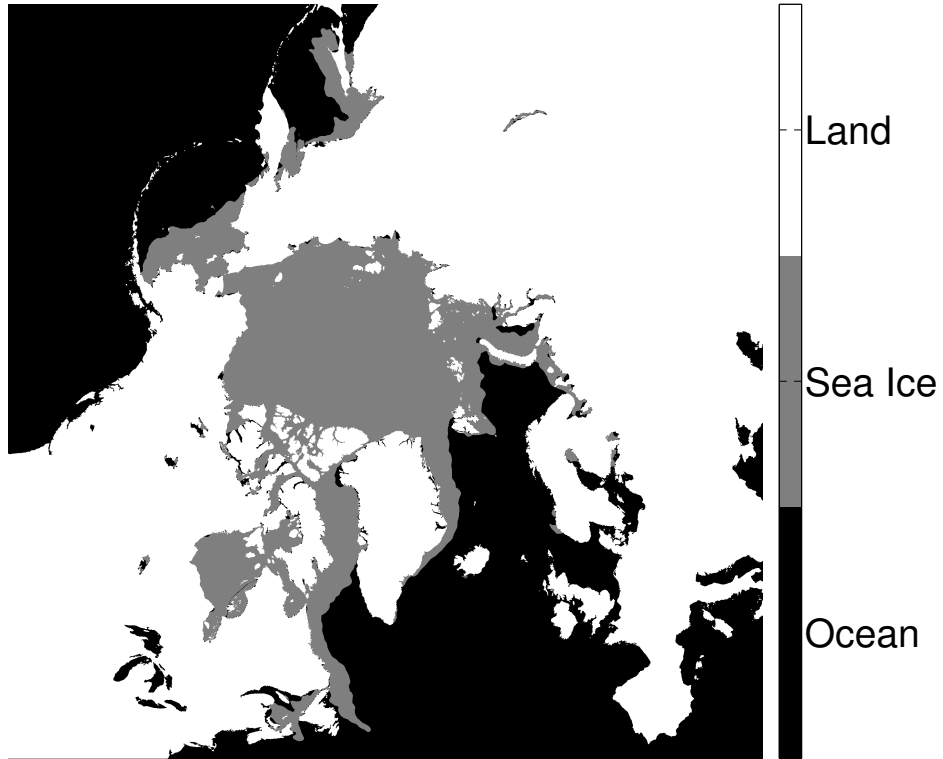
(a) Arctic
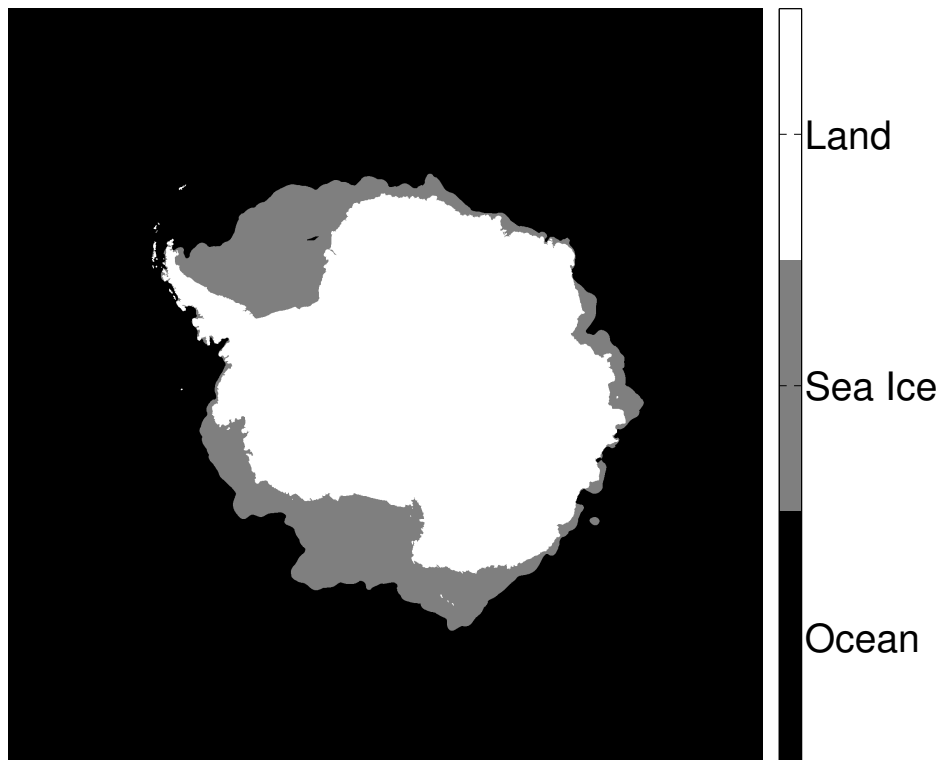
(b) Antarctic

Figure 4.13: Example ice maps for both the Arctic and the Antarctic on March 21, 2009.

Chapter 5

Validation

This chapter compares the ice maps generated by the new algorithm to other available ice maps. First, the algorithm is compared to the QSCAT RL and AMSR-E NT ice maps. Then, the new ice maps are compared to Environment Satellite (ENVISAT) Advanced Synthetic Aperture (ASAR) images.

5.1 Comparison with RL Algorithm and NT Ice Concentration Maps

This section compares the new ice maps to the QSCAT RL and AMSR-E NT ice maps. The QSCAT egg resolution RL ice maps are used because they have the same resolution as the ASCAT SIR images. On the other hand, the AMSR-E ice maps are at a lower resolution than the ASCAT ice maps. Thus, the AMSR-E images are resized using nearest-neighbor interpolation. The latitude/longitude pair of each pixel in the original AMSR-E image is compared to the latitude/longitude of each pixel in the SIR image to find the closest match. The value of the pixel from the original AMSR-E image is used.

Figure 5.1 shows the total area of sea ice in the Arctic and Antarctic using the new ice maps, the RL ice maps, and the NT AMSR-E NT 15% ice maps. The figure shows the seasonal trends of the total area of sea ice. The three algorithms follow each other closely. Next, several comparisons between these three ice mapping algorithms are performed.

The first comparison uses the percentage error in area. Figure 5.2 shows the average monthly percentage error in area between the ice maps for both the Arctic and the Antarctic. As expected, the largest error occurs during the summertime due to the melting sea ice and a smaller total area. Overall, the new algorithm has a low percentage error in area with the RL and NT ice maps.
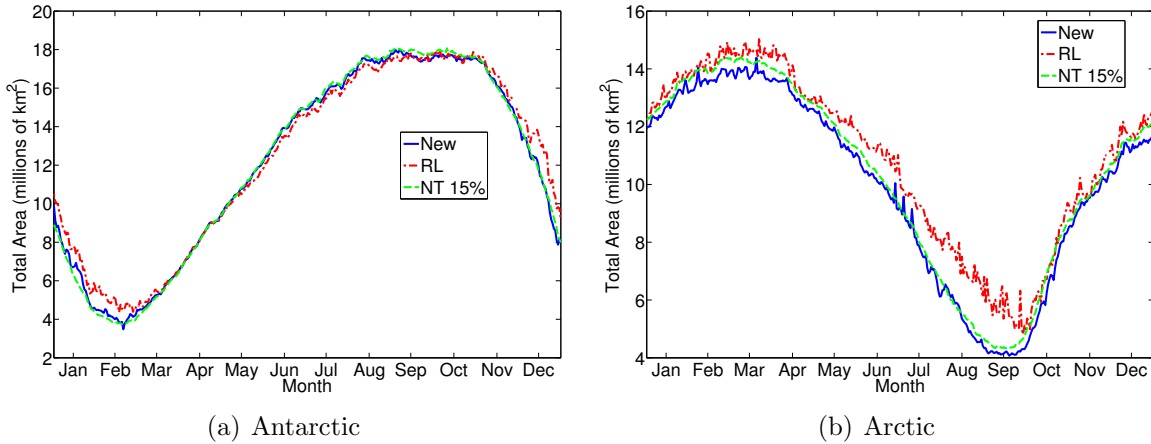
Figure 5.1: Total area of sea ice in both hemispheres for 2008 for various ice maps.
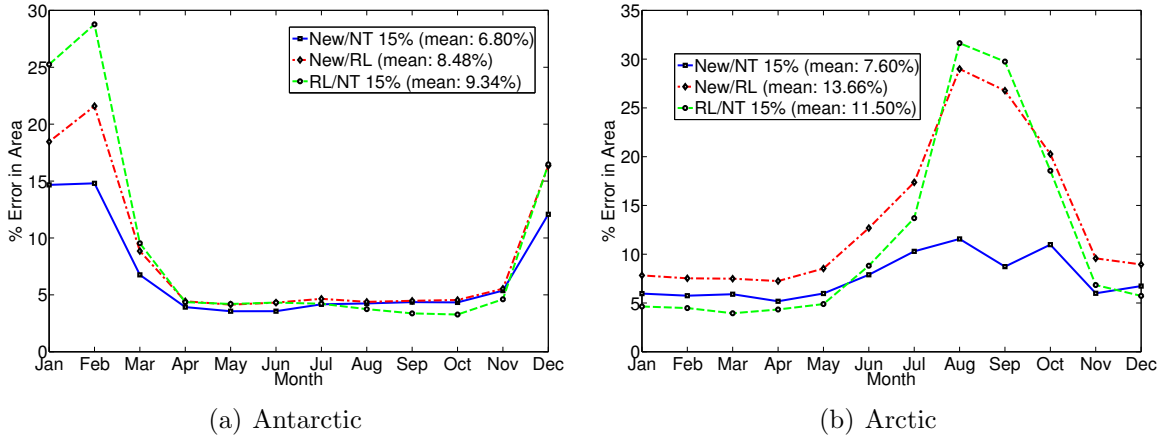

Figure 5.2: The monthly mean percentage error in area between the different algorithms for 2008.

The percentage error in area gives an overall measure of how two ice maps compare. The new Antarctic ice maps have an average error in area of 6.80% compared with the NT ice maps, while the new ice maps have an average error of 8.48% compared with the RL maps. The RL Antarctic ice maps have a large error compared to the NT maps during the summer because the large polynya in the Ross Sea is filled in during the binary processing phase. The new algorithm does not filter out the polynyas, so the large error is not present. During the winter, both the new and RL algorithms perform similarly with an average error around 5% compared to the NT maps.

The new Arctic ice maps have an average error of 7.60% compared to the NT maps, which is slightly worse than the Antarctic. The error in the Arctic does not dip as low during the winter months as the Antarctic. On the other hand, the error is not as high during the summer melt.

The percentage error in area gives a good idea of the overall performance of the algorithm. It is also useful to look at how close the ice edges are to each other. In order to objectively compare ice edges, it is necessary to first trace the ice edge from each algorithm. This is performed using the Moore neighborhood contour tracing algorithm [33].

To trace the edge, first, a binary ice map is produced with values of 1 corresponding to sea ice. Land pixels are also given a value of 1 in the Antarctic. The land is left out for the Arctic due to its geometry. Each contour in the binary image is traced using the Moore neighborhood algorithm.

The contours from two ice maps are compared by going around the contour from one ice map and finding the corresponding nearest neighbor in the other ice map. If one of the pixels from the contour falls on land, then the pixel is skipped. The latitude and longitude for the pixel on the contour and its nearest neighbor are then calculated. The great-circle distance is used to find the distance between the two latitude/longitude points.

The average of all the distances around the contour gives a good measure of how close the two ice edges are to each other. Figure 5.3 shows the average distance between the ice edges for each month. Similar to the mean percentage error in area in Figure 5.2 the distance between the ice edges depends on the season. The average distance between the new maps and the NT 15% maps is 21.91 km in the Antarctic and 18.90 km in the Arctic. Because the NT maps are gridded at 12.5 km per pixel, these distances suggest the new ice maps are within 1 to 2 pixels of the NT ice maps.

As discussed in Chapter 3, two types of errors are present in the ice maps. The first type is a missed detection, which is a pixel classified as sea ice when the pixel is actually ocean. The other type of error is a false alarm, which is a pixel classified as sea ice that is actually ocean. Figure 5.4 shows the percentage of valid pixels that are missed detections.
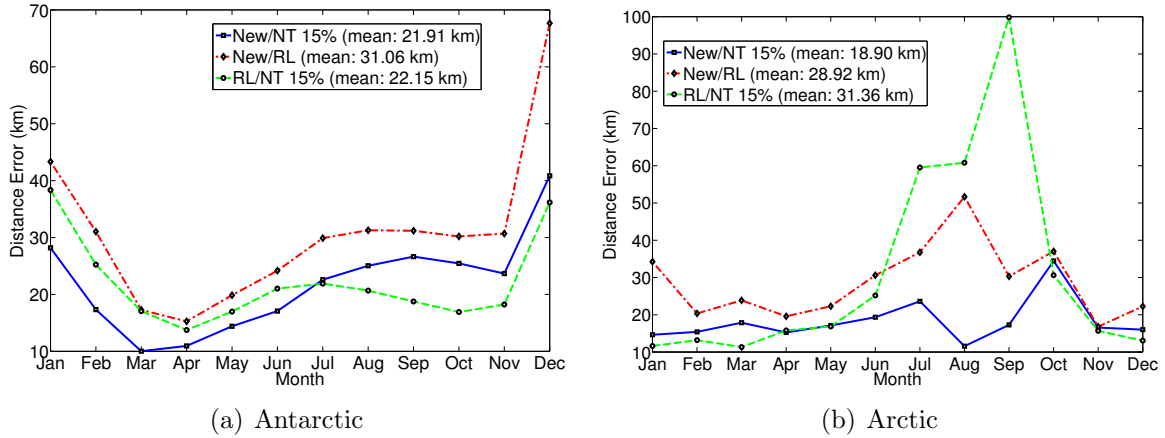
(a) Antarctic (b) Arctic

Figure 5.3: The monthly mean distance between the ice edges for the three algorithms for 2008.
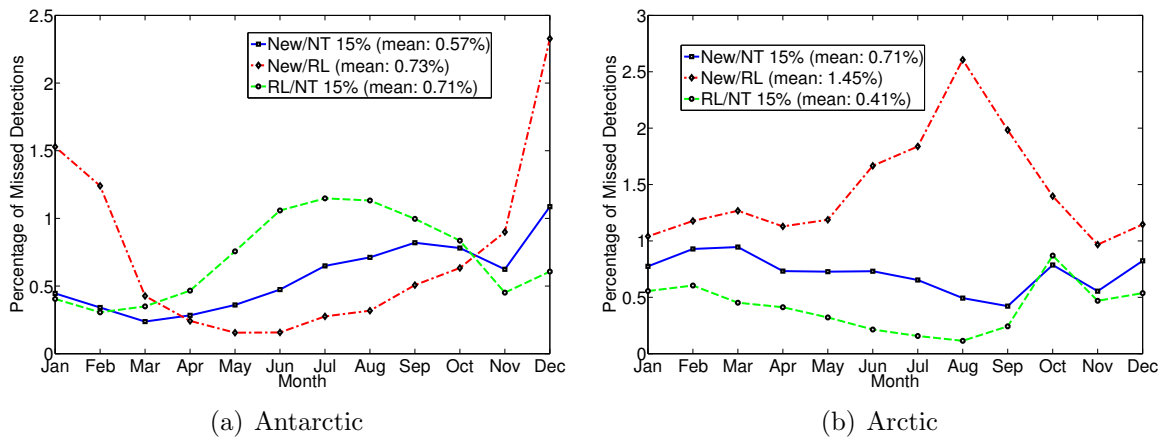

(a) Antarctic (b) Arctic

Figure 5.4: The percentage of valid pixels that are missed detections. The monthly average for 2008 is shown. Two of the plots use the NT maps as "truth", and the other plot uses RL maps as "truth"

Similarly, Figure 5.5 shows the percentage of valid pixels that are false alarms. Valid pixels are any pixels that are classified, which excludes land pixels and pixels with no data.

The new ice maps have a higher percentage of missed detections than the RL ice maps when compared to the NT 15% maps in the Arctic. On the other hand, the new ice maps have a lower percentage of false alarms in both poles. In both cases, the percentage is
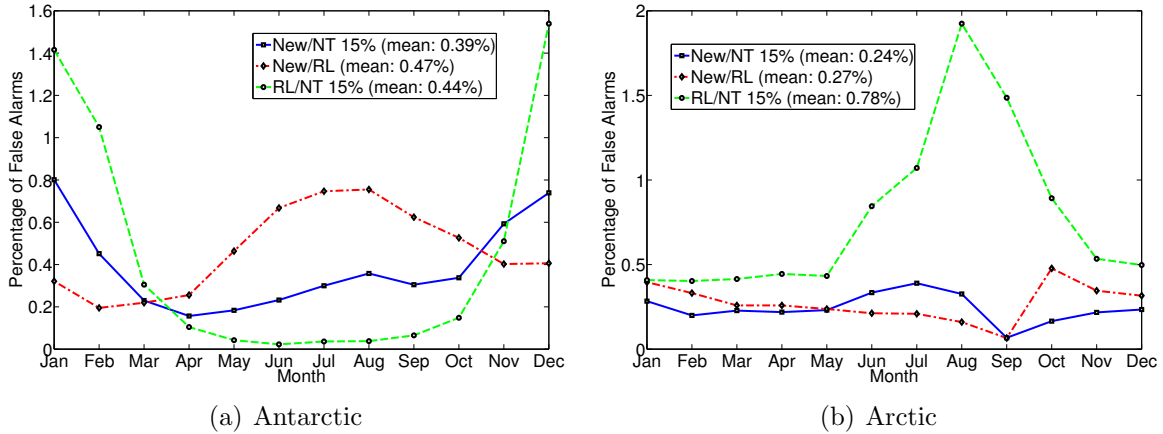
Figure 5.5: The percentage of valid pixels that are false alarms. The monthly average for 2008 is shown. Two of the plots use the NT maps as "truth", and the other plot uses RL maps as "truth".

less than one percent. This means that on average, less than one percent of the valid pixels are missed detections and less than one percent are false alarms.

The previous graphs all use the NT 15% ice concentration maps as a reference. It is also important to look at other ice concentrations. Figure 5.6 shows the average monthly ice concentration that gives the smallest percentage error in area. Figure 5.7 shows the average monthly ice concentration for the ice edge only. For both hemispheres, the concentration tends to be lower during the summer months. This is because the ice edge is more diffuse during the summer. The Arctic region has a few interesting artifacts. The RL ice maps concentration for the smallest percentage error goes to zero during the summer months. This is the only time where there is a large difference between the RL and new algorithm's concentration values. Also note that the average concentration of the ice edge is much higher for the Arctic region. This is an artifact of the difficulty in defining the ice edge for this region. The ice edge includes many areas close to land that bias the concentration to a higher value. Future work could resolve this issue by eliminating edge pixels close to land in the comparison.
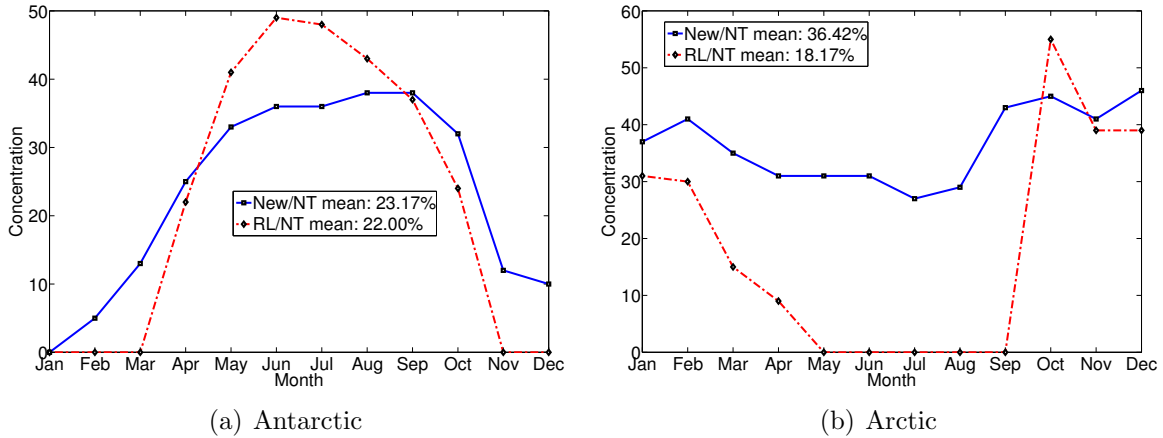
(a) Antarctic   (b) Arctic

Figure 5.6: The average monthly concentration value that produces the smallest percentage error in area.

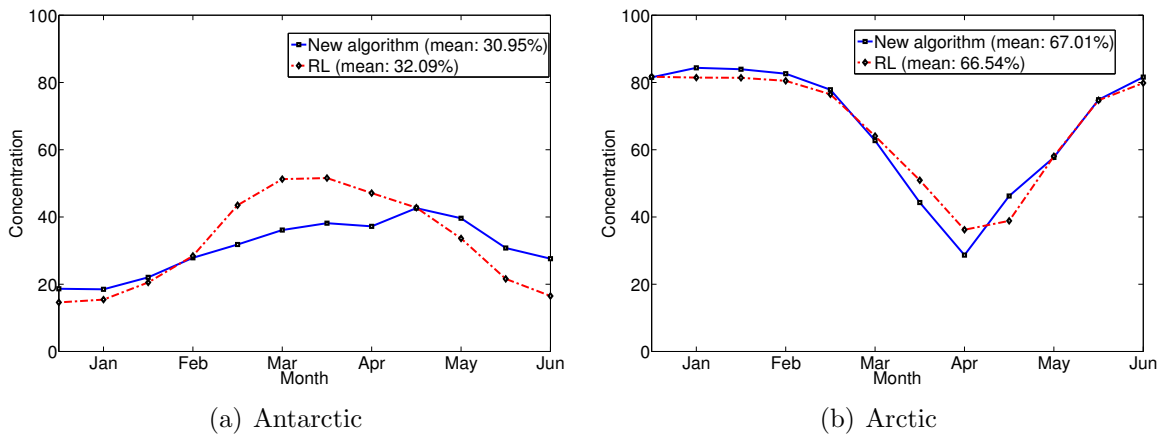(a) Antarctic   (b) Arctic

Figure 5.7: The average monthly concentration value for the ice edge in 2008.

5.2   Comparison with ENVISAT Images

The previous section gives an objective comparison of the new algorithm to the NT AMSR-E ice maps and the RL ice maps. This section compares the ice maps to high resolution SAR data. In particular, ENVISAT-ASAR images in the global-monitoring mode are employed. These images are gridded at 1 km per pixel.

In addition to the new algorithm's edge, two other ice edges are overlayed on the ENVISAT images. The first is the SSM/I NT 15% ice edge. SSM/I is used for this section because AMSR-E is not operational during the period of available ENVISAT images. The
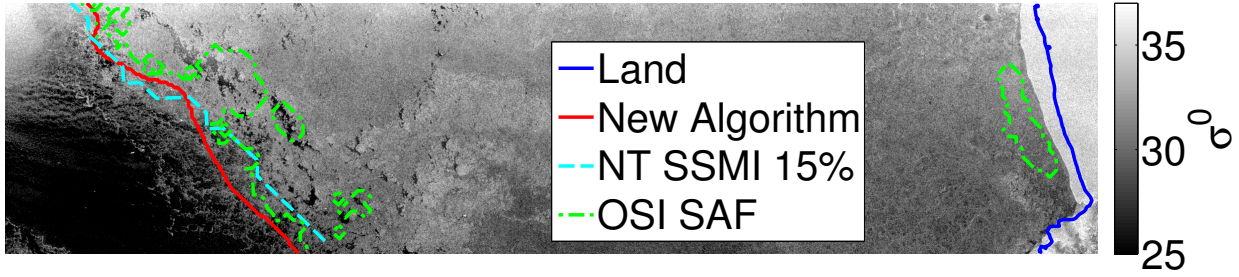
Figure 5.8: ENVISAT ASAR image in the global monitoring mode from February 21, 2012 over Antarctica. The ice edge for the new algorithm, NT SSMI 15%, and OSI SAF are all plotted. The ice edge is on the left side of the image. The new algorithm's ice edge is a little further out than the other two edges, but does appear to follow the actual edge.

NT SSM/I algorithm is the same algorithm that is used to generate the AMSR-E maps used in the previous section only with different data. However, the SSM/I maps are gridded at 25 km per pixel which is half the resolution of the AMSR-E maps.

The Ocean and Sea Ice (OSI) Satellite Application Facility (SAF) also produces an ice edge product [34]. This algorithm uses ASCAT and SSM/I to produce a sea ice map gridded at 25 km per pixel.

Figures 5.8-5.11 show the ice edge for various ice maps overlayed on the ENVISAT image. All three algorithms agree well with what appears to be the ice edge in the EN-VISAT image. Figure 5.9 includes a polynya which all three algorithms detected. The new algorithm's edge goes a little further out than the other two algorithms. This image occurs during the summer melt which the previous section showed that the ice edge tends to follow the 0% concentration. This helps validate both the new algorithm and the NT algorithm. In Figure 5.11 the edge for all three algorithms is overestimated.

5.3 Summary

This chapter validated the new algorithm with other ice maps including the NT, RL, OSI SAF ice maps. The new ice maps generally agree with the other ice maps. In the Antarctic, the new ice maps had an average percentage error in area of 6.80% with the NT
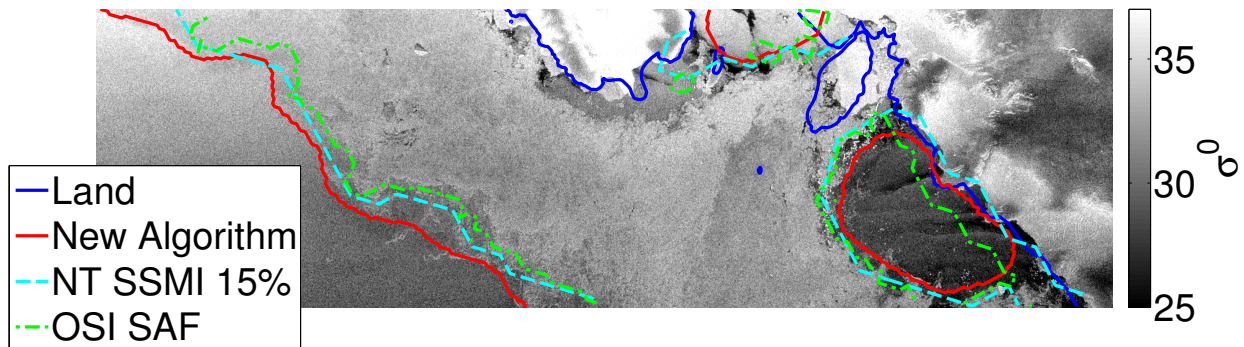
Figure 5.9: ENVISAT ASAR image in the global monitoring mode from February 21, 2012 over Antarctica. The ice edge for the new algorithm, NT SSMI 15%, and OSI SAF are all plotted. Similar to Figure 5.8, the new algorithm's ice edge is further out than the other two algorithms. In this figure, the new algorithm's edge appears to extend a little further than where the actual ice edge is located. Also note the large polynya on the right that all three algorithms detected.

Figure 5.10: ENVISAT ASAR image in the global monitoring mode from February 21, 2012 over the Arctic region. The ice edge for the new algorithm, NT SSMI 15%, and OSI SAF are all plotted. The new algorithm appears to follow the edge more closely than the other two algorithms. However, the new algorithm includes a number of small polynyas that do not actually exist.
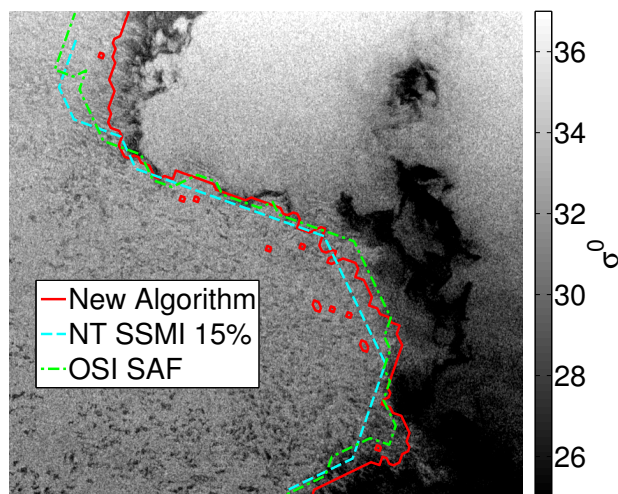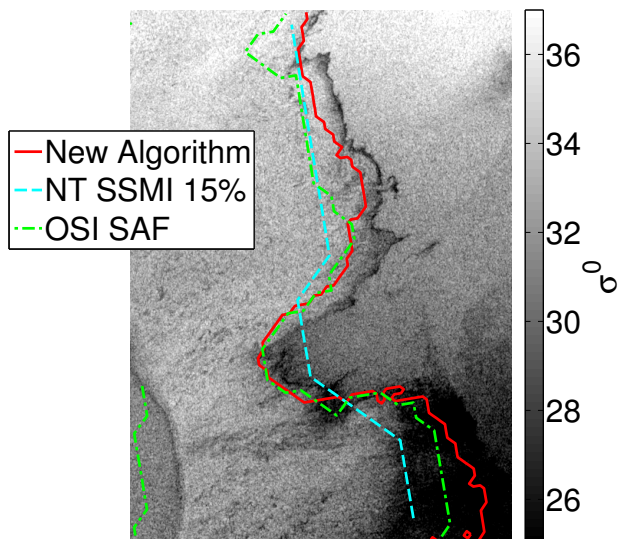
Figure 5.11: ENVISAT ASAR image in the global monitoring mode from February 21, 2012 over the Arctic region. The ice edge for the new algorithm, NT SSMI 15%, and OSI SAF are all plotted. In the bottom right of this image, all three edges appear to go beyond where the actual edge is located. This is especially apparent in the new algorithm's edge.

15% maps and an average error of 8.48% with the RL ice maps. The Arctic had an average error of 7.60% with the NT 15% maps, and 13.66% with the RL maps. When compared to the ASAR images, the new algorithm's ice edge tends to slightly overestimate the ice edge in the Antarctic and in some cases the Arctic.

Chapter 6

Conclusion

Sea ice plays an important role in the Earth's climate and ecosystem as well as many human activities. Knowledge of the ice extent can aid transportation and climate studies of the polar region. Many methods exist to detect and map the ice extent. In particular, a few algorithms have been developed that use enhanced resolution scatterometer images. These algorithms were optimized for the QSCAT instrument.

A new ice mapping algorithm is developed in Chapter 3. The new algorithm is a modified version of the QSCAT ice mapping algorithms that is optimized for ASCAT. The algorithm incorporates a Bayes decision rule to classify pixels as sea ice or ocean. The decision rule includes a prior probability which is estimated from a previous day's ice map and a thresholded image. In addition, the decision rule includes a conditional PDF which is estimated empirically from the data.

The algorithm uses two different methods to estimate the conditional PDF's. The algorithm utilizes the advantages of both methods by switching between the methods depending on the iteration. The first method assumes the PDF is Gaussian and simplifies to estimating the mean and covariance. This method minimizes false alarms and is used to detect the ice edge. The second method uses normalized histograms. This method minimizes missed detections and is used to detect polynyas.

The algorithm includes digital image processing techniques which eliminate errors and smooth the map. These techniques include: median filtering, hole filling, and dilation. The new algorithm also uses the previous day's ice map to classify areas of no data.

6.1 Contributions

This thesis includes several contributions that add to previous work on remote sensing of sea ice. A new algorithm is developed for mapping sea ice using enhanced resolution ASCAT images. The ice maps produced by the new algorithm are validated with the widely accepted NT ice maps and the RL ice maps. The contributions of the new algorithm and its validation are summarized in the following sections.

6.1.1 Normalized Difference Images

The new algorithm incorporates a new type of image known as the normalized difference image. The normalized difference uses ASCAT's fore and aft antennas. It is a measure of the azimuth angle dependence of a region. This new image provides high contrast between sea ice and ocean. It is thresholded to assist in the generation of the PPM's, and it is also used in the decision rule as one of the features.

6.1.2 Prior Probability Map

A method is developed to generate prior probability maps. These maps assign a prior probability to each pixel in the image. The maps allow the decision rule to include a spatial dependence, and the maps constrain the sea ice movement from day to day. To prevent errors from propagating through several days, a thresholded image is employed.

6.1.3 Conditional PDF Methods

A study is performed to analyze two methods to estimate the conditional PDF used in the decision rule. It is determined that both the Gaussian and histogram method have advantages which are useful to the algorithm. Thus, both methods are employed to create the sea ice map. The resulting sea ice maps are able to detect polynyas without a large increase in false alarms.

6.1.4 Algorithm Tuning

A number of parameters for the new algorithm are tuned to achieve better performance. The algorithm is tuned to the NT 15% concentration ice maps. The NT ice maps

have been used for a number of years and are frequently used as a benchmark for other ice mapping algorithms.

6.1.5 Validation of the New Ice Maps

The new ice maps are validated with the NT and RL ice maps. A number of comparisons are made with these ice maps that show the new ice maps are consistent with the other ice maps. These comparisons include: percentage error in area, average distance in ice edge, percentage of missed detections, percentage of false alarms, concentration value that gives the lowest percentage error in area, and average concentration of the ice edge. In addition, the RL QSCAT ice maps are also compared to the NT ice maps. This provides a more complete validation of the RL algorithm.

6.2 Future Research

The research presented in this thesis provides a number of opportunities for future work. Several areas of possible future research are discussed in the following sections.

6.2.1 Algorithm Tuning

Not all of the parameters for the new algorithm have been optimized. This includes the number of iterations, which images to use on each iteration, the weighting of the **d** PPM versus the previous day's PPM, and the size of the Gaussian kernel. In addition, this thesis only used the AMSR-E NT 15% ice maps to tune the algorithm. Future work could tune the algorithm with different ice maps.

6.2.2 OSCAT

The Oceansat-2 Scatterometer (OSCAT) is a more recent scatterometer that is a clone of QSCAT. The new algorithm could be applied to OSCAT (as well as QSCAT). Potentially the Polarization Ratio (PR) image could be used as the thresholded image for the PPM's. In addition, the increased coverage of OSCAT means that only one day images are necessary.

6.2.3 Multi-Sensor Sea Ice Mapping

Although parts of the algorithm are tied to ASCAT itself (especially the images), the underlying algorithm is not tied to ASCAT only. The previous section discussed using the algorithm on OSCAT. The algorithm could be easily extended to use multiple sensors. This could include combining OSCAT and ASCAT or even a radiometer. Multiple sensors could potentially be combined by first creating ice maps individually, and then combining in some sort of fashion (maybe a weighted average). The sensors could also be combined by incorporating the different sensor's images for each iteration.

6.2.4 Normalized Difference Image Study

A study involving azimuth angle dependence could utilize the normalized difference images. A study involving both sea ice and land areas could use these images.

6.2.5 C-Band to Ku-Band Study

Recall that ASCAT is at C-band and QSCAT is at Ku-band. The two sensors have overlap for more than a year. The new ice maps could be used in a study to compare C-band properties of sea ice to Ku-band.

6.2.6 Sea Ice Type Classification

The new ice maps could be used as an input to classify sea ice type. Sea ice can broadly be classified into first year and multiyear ice. In addition, sea ice can be classified into many other types that help to describe many characteristics of the ice.

Bibliography

[1] F. Carsey, *Microwave Remote Sensing of Sea Ice.* American Geophysical Union, 1992, no. 68. 1, 2

[2] "The Cryosphere: Where the World is Frozen," Sep. 2011, http://www.nsidc.org/cgi-bin/words/glossary.pl. 2

[3] T. Markus and D. Cavalieri, "An Enhancement of the NASA Team Sea Ice Algorithm," *IEEE Transactions on Geoscience and Remote Sensing*, vol. 38, no. 3, pp. 1387–1398, 2002. 2, 13, 15

[4] J. Comiso and Goddard Space Flight Center, *SSM/I Sea Ice Concentrations Using the Bootstrap Algorithm.* National Aeronautics and Space Administration, Goddard Space Flight Center, 1995, vol. 1380. 2, 13

[5] Q. Remund and D. Long, "Sea Ice Extent Mapping Using Ku Band Scatterometer Data," *Journal of Geophysical Research*, vol. 104, no. C5, p. 11515, 1999. 3, 13, 15, 16, 18, 22, 23, 37

[6] H. Anderson and D. Long, "Sea Ice Mapping Method for Seawinds," *IEEE Transactions on Geoscience and Remote Sensing*, vol. 43, no. 3, pp. 647–657, 2005. 3, 11, 13, 15, 16, 19, 22, 25, 30, 31, 37

[7] J. Haarpaintner, R. Tonboe, D. Long, and M. Van Woert, "Automatic detection and validity of the sea-ice edge: an application of enhanced-resolution QuikScat/SeaWinds data," *IEEE Transactions on Geoscience and Remote Sensing*, vol. 42, no. 7, pp. 1433–1443, 2004. 3, 13, 15, 16, 37

[8] M. Belmonte Rivas and A. Stoffelen, "New Bayesian Algorithm for Sea Ice Detection With QuikSCAT," *IEEE Transactions on Geoscience and Remote Sensing*, no. 99, pp. 1–8, 2011. 3, 13, 37

[9] J. Park, W. Jones, and J. Zec, "Sea Ice Classification Using a Neural Network Algorithm for NSCAT," in *Geoscience and Remote Sensing Symposium, 1999. IGARSS'99 Proceedings. IEEE 1999 International*, vol. 2. IEEE, 1999, pp. 1040–1043. 3, 13

[10] F. Gohin and C. A., "A first try at identification of sea ice using the three beam scatterometer of ERS-1," *International Journal of Remote Sensing*, vol. 15, no. 6, pp. 1221–1228, 1994. 3, 13, 18, 22

[11] D. Long, P. Hardin, and P. Whiting, "Resolution Enhancement of Spaceborne Scatterometer Data," *IEEE Transactions on Geoscience and Remote Sensing*, vol. 31, no. 3, pp. 700–715, 1993. 3, 11

[12] D. Early and D. Long, "Image Reconstruction and Enhanced Resolution Imaging from Irregular Samples," *IEEE Transactions on Geoscience and Remote Sensing*, vol. 39, no. 2, pp. 291–302, 2001. 3, 11

[13] J. Figa-Saldana, J. Wilson, E. Attema, R. Gelsthorpe, M. Drinkwater, and A. Stoffelen, "The Advanced Scatterometer (ASCAT) on the meteorological operational (MetOp) platform: A follow on for European wind scatterometers," *Canadian Journal of Remote Sensing*, vol. 28, no. 3, pp. 404–412, 2002. 7, 8

[14] M. Spencer, C. Wu, and D. Long, "Tradeoffs in the Design of a Spaceborne Scanning Pencil Beam Scatterometer: Application to SeaWinds," *IEEE Transactions on Geoscience and Remote Sensing*, vol. 35, no. 1, pp. 115–126, 1997. 9

[15] I. Ashcraft and D. Long, "The spatial response function of seawinds backscatter measurements," in *Proceedings of SPIE*, vol. 5151, 2003, pp. 609–618. 8

[16] J. Heinrichs, D. Cavalieri, and T. Markus, "Assessment of the AMSR-E Sea Ice-Concentration Product at the Ice Edge Using RADARSAT-1 and MODIS Imagery," *IEEE Transactions on Geoscience and Remote Sensing*, vol. 44, no. 11, pp. 3070–3080, 2006. 10, 16, 37

[17] T. Kawanishi, T. Sezai, Y. Ito, K. Imaoka, T. Takeshima, Y. Ishido, A. Shibata, M. Miura, H. Inahata, and R. Spencer, "The Advanced Microwave Scanning Radiometer for the Earth Observing System (AMSR-E), NASDA's contribution to the EOS for global energy and water cycle studies," *IEEE Transactions on Geoscience and Remote Sensing*, vol. 41, no. 2, pp. 184–194, 2003. 10

[18] L. Breivik and E. S., "Upgrade of the OSI SAF Sea Ice Edge and Sea Ice Type Products - Introduction of ASCAT," September 2009, [Online]. Available: http://saf.met.no/docs/report_osisaf_seaice_edge_type_validation.pdf. 10, 15

[19] P. Yu, D. Clausi, and S. Howell, "Fusing AMSR-E and QuikSCAT Imagery for Improved Sea Ice Recognition," *IEEE Transactions on Geoscience and Remote Sensing*, vol. 47, no. 7, pp. 1980–1989, 2009. 10

[20] I. Ashcraft and D. Long, "Azimuth variation in microwave backscatter over the Greenland ice sheet," in *Geoscience and Remote Sensing Symposium, 2001. IGARSS'01. IEEE 2001 International*, vol. 4. IEEE, 2001, pp. 1779–1781. 11

[21] D. Long and M. Drinkwater, "Azimuth variation in microwave scatterometer and radiometer data over Antarctica," *IEEE Transactions on Geoscience and Remote Sensing*, vol. 38, no. 4, pp. 1857–1870, 2000. 11

[22] Q. Remund, D. Long, and M. Drinkwater, "An iterative approach to multisensor sea ice classification," *IEEE Transactions on Geoscience and Remote Sensing*, vol. 38, no. 4, pp. 1843–1856, 2000. 11

[23] K. Stuart and D. Long, "Iceberg size and orientation estimation using SeaWinds," in *Geoscience and Remote Sensing Symposium (IGARSS), 2010 IEEE International*. IEEE, 2010, pp. 2394–2397. 11

[24] D. Long and P. Hardin, "Vegetation studies of the Amazon Basin using enhanced resolution Seasat scatterometer data," *IEEE Transactions on Geoscience and Remote Sensing*, vol. 32, no. 2, pp. 449–460, 1994. 11

[25] J. Grandell, J. Johannessen, and M. Hallikainen, "Development of a Synergetic Sea Ice Retrieval Method for the ERS-1 AMI Wind Scatterometer and SSM/I Radiometer," *IEEE Transactions on Geoscience and Remote Sensing*, vol. 37, no. 2, pp. 668–679, 1999. 15

[26] Onstott, R.G., Shuchman R.A., "SAR Measurements of Sea Ice," in *Synthetic Aperture Radar Marine User's Manual*, Jackson, C.R., Apel, J.R., Ed., 2005, pp. 81–115. 16

[27] F. Ulaby, R. Moore, and A. Fung, *Microwave remote sensing: Active and passive. Volume 2- Radar remote sensing and surface scattering and emission theory.* Artech House, Inc., 1982. 17

[28] D. Early and D. Long, "Azimuthal Modulation of C-band Scatterometer σ^0 over Southern Ocean Sea Ice," *IEEE Transactions on Geoscience and Remote Sensing*, vol. 35, no. 5, pp. 1201–1209, 1997. 17

[29] Q. Remund and D. Long, "Sea Ice Mapping Algorithm for QuikScat and SeaWinds," in *Geoscience and Remote Sensing Symposium Proceedings, 1998. IGARSS'98. 1998 IEEE International*, vol. 3. IEEE, 1998, pp. 1686–1688. 18

[30] Q. Remund, "Multisensor Microwave Remote Sensing in the Cryosphere," *Ph.D. Dissertation, Brigham Young University*, August 2000. 22

[31] D. Early and D. Long, "Ice Classification in the Southern Ocean Using ERS-1 Scatterometer Data," in *Geoscience and Remote Sensing, 1997. IGARSS'97. Remote Sensing-A Scientific Vision for Sustainable Development., 1997 IEEE International*, vol. 4. IEEE, 1997, pp. 1838–1840. 22

[32] L. Vincent, "Morphological Grayscale Reconstruction in Image Analysis: Applications and Efficient Algorithms," *IEEE Transacations on Image Processing*, vol. 2, no. 2, pp. 176–201, 1993. 34

[33] S. Michael and J. Sammon, *Practical Algorithms for Image Analysis.* Cambridge University Press, 2000. 48

[34] "Sea Ice Product Manual," April 2011, [Online]. Available: http://saf.met.no/docs/osisaf_ss2_pum_ice-conc-edge-type_v3p7.pdf. 52

Appendix A

Nomenclature

$\mathcal{A}$	The $\mathcal{A}$ image produced from the SIR algorithm
AMSR-E	Advance Microwave Scanning Radiometer for the Earth Observing System
ASAR	Advanced Synthetic Aperture Radar
ASCAT	Advanced Scatterometer
$\mathcal{B}$	The $\mathcal{B}$ image produced from the SIR algorithm
$\mathbf{d}$	Normalized difference image
e	Emissivity
ENVISAT	Environmental Satellite
h-pol	Horizontal polarization
NRCS	Normalized Radar Cross Section (σ^0)
NT	NASA Team
PPM	Prior Probability Map
QSCAT	QuikSCAT
RL	Remund Long algorithm
SAR	Synthetic Aperture Radar
SIR	Scatterometer Image Reconstruction
SSM/I	Special Sensor Microwave Imager
T_B	Brightness Temperature
V	The standard deviation image produced from the SIR algorithm
v-pol	Vertical polarization

Appendix B

Prior Probability Maps Using Thresholded Images

The **d** prior probability map (PPM) uses a binary mask of the sea ice. The binary mask is generated from a thresholded **d** image with a median filter. The binary mask needs to accurately map the ice extent so that the PPM is an accurate prior probability for each pixel.

This appendix considers several values for the threshold and the size of the median filter in order to determine the optimum values. The binary masks are compared with the AMSR-E NT 15% ice concentration maps to determine which threshold and median filter size most accurately map the ice extent.

Figures B.1, B.2, B.3, B.4, B.5, and B.6 show the percentage error in area between the binary masks and the NT 15% concentration maps. Each figure plots several threshold values for a single median filter size. The seasonal trends of the sea ice are apparent in the figures. During, the summer time, the percentage error is significantly higher. Overall,a threshold of 0.15 provides the best results in the Antarctic, and a threshold of 0.125 provides the best results in the Arctic.

(a) Antarctic   (b) Arctic
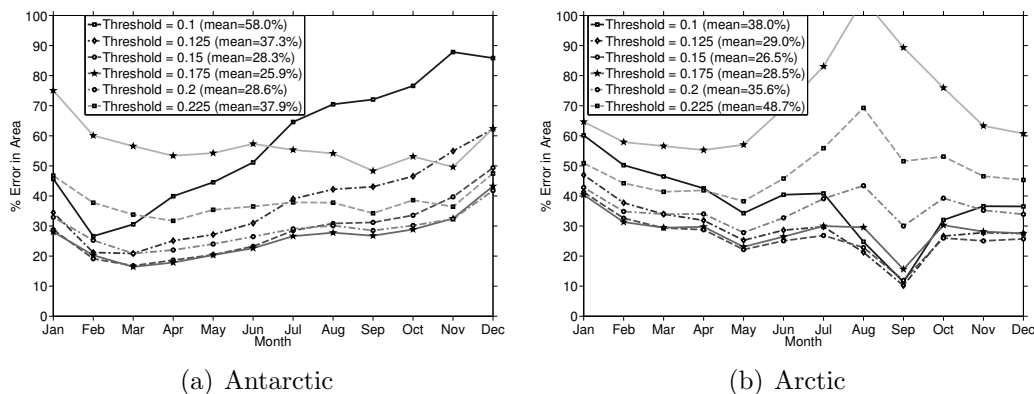
Figure B.1: Percentage error in area between the thresholded **d** images and the NT 15% ice maps with a median filter of size 0.
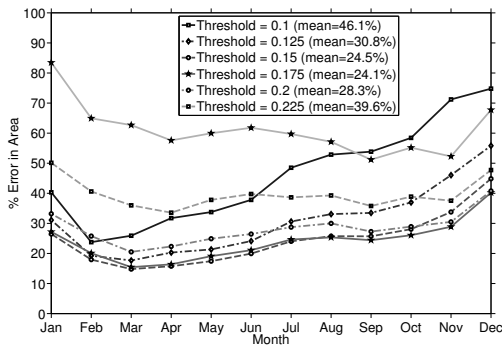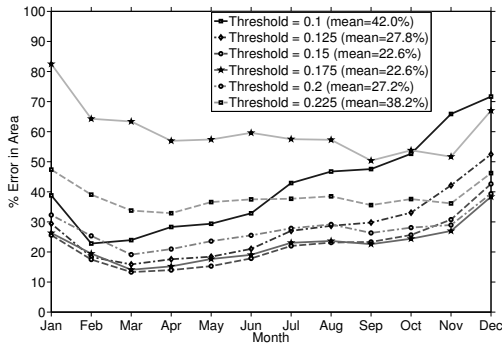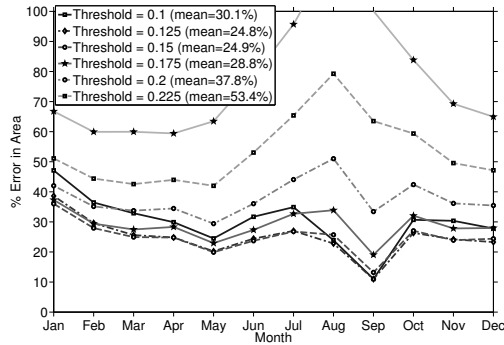
(a) Antarctic
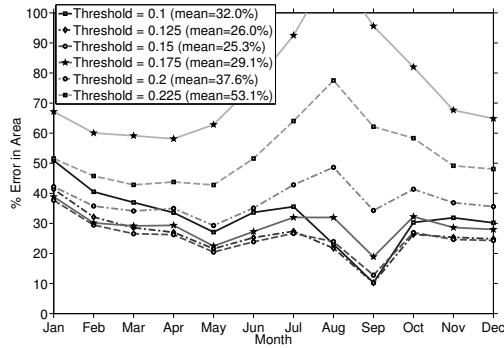
(b) Arctic

Figure B.2: Percentage error in area between the thresholded **d** images and the NT 15% ice maps with a median filter of size 5.
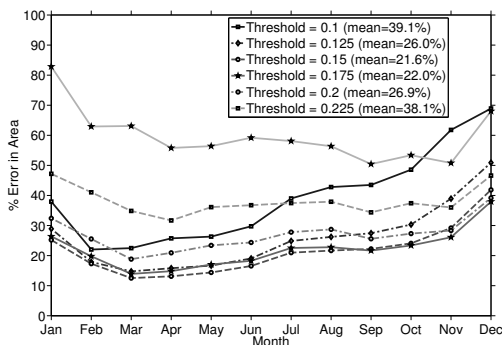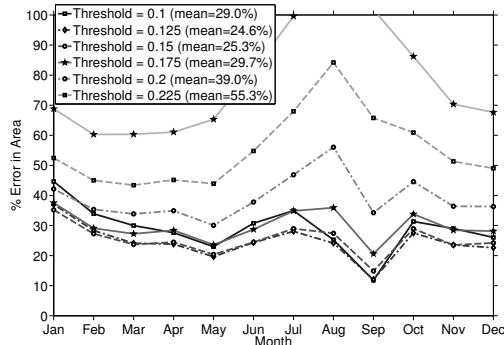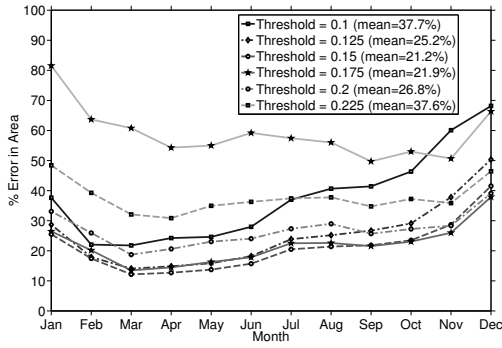

(a) Antarctic

(b) Arctic

Figure B.3: Percentage error in area between the thresholded **d** images and the NT 15% ice maps with a median filter of size 10.
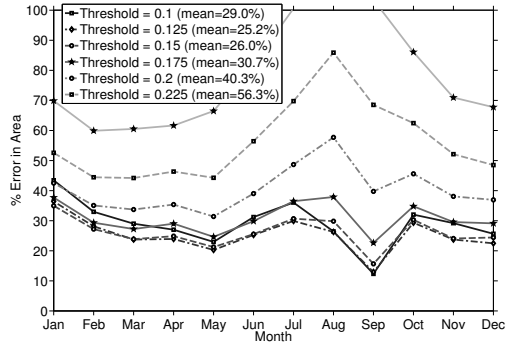

(a) Antarctic

(b) Arctic

Figure B.4: Percentage error in area between the thresholded **d** images and the NT 15% ice maps with a median filter of size 15.
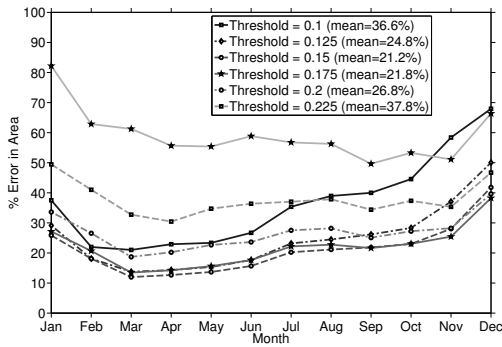
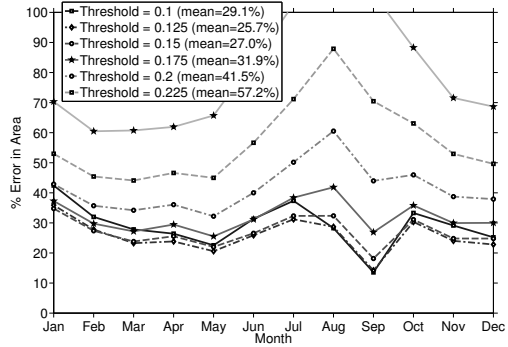(a) Antarctic   (b) Arctic

Figure B.5: Percentage error in area between the thresholded **d** images and the NT 15% ice maps with a median filter of size 20.

(a) Antarctic   (b) Arctic

Figure B.6: Percentage error in area between the thresholded **d** images and the NT 15% ice maps with a median filter of size 25.